

Is spontaneous generation of coherent baroclinic flows possible?

Nikolaos A. Bakas^{1†} and Petros J. Ioannou²

¹Laboratory of Meteorology and Climatology, Department of Physics, University of Ioannina, Ioannina, Greece

²Department of Physics, National and Kapodistrian University of Athens, Athens, Greece

(Received xx; revised xx; accepted xx)

Geophysical turbulence is observed to self-organize into large-scale flows such as zonal jets and coherent vortices. Previous studies on barotropic beta-plane turbulence, a simple model that retains the basic self-organization dynamics, have shown that coherent flows emerge out of a background of homogeneous turbulence as a bifurcation when the turbulence intensity increases and the emergence of large scale flows has been attributed to a new type of collective, symmetry breaking instability of the statistical state dynamics of the turbulent flow. In this work we extend the analysis to stratified flows and investigate turbulent self-organization in a two-layer fluid with no imposed mean north-south thermal gradient and turbulence supported by an external random stirring. We use a second order closure of the statistical state dynamics (S3T) with an appropriate averaging ansatz that allows the identification of statistical turbulent equilibria and their structural stability. The bifurcation of the statistically homogeneous equilibrium state to inhomogeneous equilibrium states comprising of zonal jets and/or large scale waves when the energy input rate of the excitation passes a critical threshold is analytically studied. The theory predicts that when the flow transitions to a statistical state with large-scale structures, these states are barotropic if the scale of excitation is larger than the deformation radius. Mixed barotropic-baroclinic states with jets and/or waves arise when the excitation is at scales shorter than the deformation radius with the baroclinic component of the flow being subdominant for low energy input rates and non-significant for higher energy input rates. The results of the S3T theory are compared to nonlinear simulations. The theory is found to accurately predict both the critical transition parameters and the scales of the emergent structures but underestimates their amplitude.

Key words:

1. Introduction

Large scale flows like the zonal jets and the large-scale vortices of the gaseous planets are a common feature of the turbulent state in planetary atmospheres (Ingersoll 1990; Maximenko *et al.* 2005; Galperin *et al.* 2014). There are two type of theories that have been advanced for the emergence and maintenance of these flows: the deep origin theories that propose that the origin of the jets is due to Reynolds stresses arising from convection from the interior of the planet (cf. Busse (1976); Kaspi *et al.* (2009)) and theories that posit that the jets have a shallow origin and emerge when large-scale atmospheric turbulence

† Email address for correspondence: nbakas@uoi.gr

evolves in the presence of latitudinal variations of the Coriolis parameter on the surface of the planet (the planetary β effect) (Williams 1978, 2003; Cho & Polvani 1996; Kaspi & Flierl 2007; Showman 2007; Scott & Polvani 2007; Liu & Schneider 2010; Thomson & McIntyre 2014). Comprehensive review of these theories can be found in Vasavada & Showman (2005) and in Sánchez-Lavega *et al.* (2019).

One of the simplest models that has been widely studied is the organization of large scale structures in barotropic β -plane turbulence (cf. Rhines (1975); Vallis & Maltrud (1993)). Recently, following theoretical predictions (Farrell & Ioannou 2007), direct numerical simulations of forced-dissipative barotropic turbulence on a beta-plane indicated that large-scale coherent flows could emerge through a symmetry breaking bifurcation of the turbulent flow: as dissipation or turbulence intensity varies, the homogeneity of the flow is broken by the spontaneous emergence of zonal jets and large-scale waves and the large-scale structures are supported at finite amplitude by the turbulent eddies through shear straining (Srinivasan & Young 2012; Bakas & Ioannou 2013a; Constantinou *et al.* 2014a). Similar numerical calculations on a stratified two-layer β -plane channel with no temperature gradient across the channel have indicated that β -plane turbulence can maintain large scale jets with vary small baroclinic component (Farrell & Ioannou 2017). In this work we extend the analysis to stratified two-layer flows and address the following question: in the absence of temperature gradients can externally forced turbulence in a two-layer stratified flow support turbulent equilibria in which large scale baroclinic coherent flows are sustained at finite amplitude? Or are the large scale flows that emerge necessarily barotropic?

To address the emergence of large scale structure in turbulence, a new point of view was recently advanced. Through analysis of the Statistical State Dynamics (SSD) of the flow, that is of the dynamics that governs the evolution of the flow statistics, a new type of collective instability was revealed and it was proposed that emergence of large scale structure resulted from this symmetry breaking instability (Farrell & Ioannou 2003, 2007; Srinivasan & Young 2012; Parker & Krommes 2013; Bakas & Ioannou 2013a; Parker & Krommes 2014). Analysis of the SSD and the resulting instability is only possible through a closure assumption for the dynamics, as a straightforward calculation leads to an infinite hierarchy of equations for the moments and is therefore intractable (Hopf 1952; Kraichnan 1964; Frisch 1995). There is now a large number of studies of barotropic turbulence (Farrell & Ioannou 2007; Marston 2010; Srinivasan & Young 2012), shallow-water turbulence (Farrell & Ioannou 2009a), baroclinic turbulence (DelSole 1996; Farrell & Ioannou 2008, 2019; Marston *et al.* 2016), turbulence in pipe flows (Constantinou *et al.* 2014b; Farrell *et al.* 2016, 2017), turbulence in a convectively unstable flows (Herring 1963; Fitzgerald & Farrell 2014; Ait-Chaalal *et al.* 2016) and turbulence in plasma and astrophysical flows (Farrell & Ioannou 2009b; Tobias *et al.* 2011; Parker & Krommes 2013) providing evidence that whenever there is a coherent flow coexisting with the turbulent field, the SSD can be accurately captured by a second-order closure. Such closures of the SSD are either termed Stochastic Structural Stability Theory (S3T) (Farrell & Ioannou 2003) or second-order cumulant expansion (CE2) (Marston *et al.* 2008).

At first sight the success of a second order closure is surprising. Consider for example the case of zonal jets supported by barotropic turbulence. The question is whether the quasi-linear eddy-mean flow interaction, which represents shearing of the eddies by the jet, dominates the disruptive effects of the eddy-eddy interactions that are represented in the higher order cumulants. Close to the bifurcation point of jet emergence, the mean flow shear is infinitesimal and presumably the eddy-eddy interactions dominate and the quasi-linear interaction is inadequate to form jets (cf. Srinivasan & Young (2012); Frishman & Herbert (2018)). Also, in highly supercritical regimes and in the limit of high

turbulence intensity the eddy-eddy interactions may dominate and the turbulence may become strongly diffusive (Held & Larichev 1996). However, recent studies have provided evidence that the S3T dynamics are dominant both at the first bifurcation point and at reasonably high supercriticalities.

Close to the bifurcation point of jet emergence, a second-order closure was shown to be extremely accurate if the dynamics of coherent large-scale waves that significantly influence the flow in this regime are suppressed (Constantinou *et al.* 2014a) or are accounted for (Bakas & Ioannou 2013a). In addition, Bakas & Ioannou (2013b) and Bakas *et al.* (2015) studied in detail the eddy-mean flow dynamics underlying jet formation. They showed that an infinitesimal jet perturbation can influence the stochastically forced eddies and induce eddy vorticity fluxes that can be interpreted as resulting from shearing of wave-packets by the infinitesimal jet. They also found in this regime in which the eddies are dissipated before they are sheared over by the weak jet, that the induced fluxes are up-gradient leading to a positive feedback loop and to exponential growth of the jet. It is the existence of this exponential instability that underlies the success of the S3T predictions at the bifurcation points.

Several studies have identified the strongly non-linear regime using a single non-dimensional parameter: the zonostrophic parameter R_β that measures the ratio of the Rhines scale over the scale where the isotropic energy cascade gets anisotropized by β (Galperin *et al.* 2006). The Earth’s atmosphere is estimated to have $R_\beta = 1.6$ while Jupiter’s and Saturn’s jets are estimated to have $R_\beta = 5$ (Galperin *et al.* 2014). It has been confirmed that the S3T approximations extends at least up to $R_\beta = 2.5$. Bakas & Ioannou (2019) performed numerical experiments within the zonostrophic regime at $R_\beta = 2.5$ and demonstrated that the scale of the emergent structures is well captured by a second order closure while there are some quantitative differences in the intensity of the flows. This demonstrated that even though the eddy-eddy interactions are not small and may contribute to added eddy diffusion in the mean dynamics they do not affect the S3T collective instability mechanism that supports the large-scale flows. Scott & Dritschel (2012) were able to perform simulations at even higher R_β and have demonstrated that well formed potential vorticity (PV) staircases form when $R_\beta \geq 10$. The validity of the S3T dynamics in the PV staircase regime at these values of R_β has not been checked yet.

S3T has also another important theoretical advantage. The turbulent equilibria and more importantly their instability that can lead to transitions in the turbulent flow have analytic expression only in the SSD. The reason is that in turbulent simulations the Reynolds stresses have large fluctuations and the mean drift in the Reynolds stresses which is responsible for the emergence of large-scale structure is not discernible. As a result, only a framework such as S3T allows for the analytic treatment of these turbulence-mean flow instabilities and can lead to a more comprehensive understanding of turbulent bifurcations. For barotropic beta-plane turbulence it was shown that jets (Farrell & Ioannou 2007; Srinivasan & Young 2012) and large-scale waves (Bakas & Ioannou 2014) emerge as the statistical equilibrium of homogeneous turbulence becomes unstable. This instability, was shown to be the generalization of modulational instability in stochastically forced dissipative flows (Parker & Krommes 2015; Bakas *et al.* 2015).

In this work, we undertake the task of presenting the analytical S3T theory for a stratified fluid on a β -plane addressing the following: (i) what type of large scale flows emerge and are sustained at finite amplitude in a turbulent stratified atmosphere that is homogeneous both in the horizontal and the vertical? (ii) Since in this setting, the turbulence injection scale is not necessarily the Rossby radius of deformation as is for example the classical case of baroclinic instability, how does the energy flow depend on the ratio of the turbulence injection scale to the deformation radius?

We use a two-layer model on a β -plane that allows both analytic treatment of the dynamics and numerical integration of the high dimensional SSD of the flow. We choose to maintain this turbulent field in the simplest manner by introducing a homogeneous and isotropic stochastic excitation that drives the turbulence and dissipation is represented as linear dissipation of potential vorticity. The structure of the stochastic excitations is not important so long as it maintains the observed amplitude of turbulence given that the anisotropy of the turbulence is induced by its interaction with the mean flow. We first present numerical simulations of the turbulent flow that demonstrate the regime transitions in the turbulent flow and identify the scales and characteristics of the emergent structures. We then derive the SSD of the flow under a second-order closure with the assumption that the average for defining the statistical moments is coarse-graining over fast time scales. We address the instability of the homogeneous equilibrium of the SSD for a wide range of parameters and the properties of the unstable modes that represent the emerging structures. We then study the equilibration of the structure forming instability and the coherent structures supported at finite amplitude. Finally, we compare the predictions of the S3T theory against the direct numerical simulations of the turbulent flow and showcase its validity.

2. Numerical simulations of the turbulent flow

Consider a quasi-geostrophic baroclinic two-layer fluid on an infinite beta-plane. The upper and lower layers are denoted with subscripts 1 and 2, have equal depth, $H/2$, and densities ρ_1 and ρ_2 with $\rho_2 > \rho_1$. The quasi-geostrophic dynamics governing the evolution of the barotropic $\tilde{\psi} = (\psi_1 + \psi_2)/2$ and the baroclinic $\tilde{\theta} = (\psi_1 - \psi_2)/2$ streamfunction is:

$$\partial_{\tilde{t}}\tilde{\zeta} + J(\tilde{\psi}, \tilde{\zeta}) + J(\tilde{\theta}, \tilde{\Delta}\tilde{\theta}) + \tilde{\beta}\partial_{\tilde{x}}\tilde{\psi} = -\tilde{r}\tilde{\zeta} + \tilde{\xi}^{\psi}, \quad (2.1)$$

$$\partial_{\tilde{t}}\tilde{\eta} + J(\tilde{\psi}, \tilde{\eta}) + J(\tilde{\theta}, \tilde{\zeta}) + \tilde{\beta}\partial_{\tilde{x}}\tilde{\theta} = -\tilde{r}\tilde{\eta} + \tilde{\xi}^{\theta}, \quad (2.2)$$

where $\tilde{\Delta} \stackrel{\text{def}}{=} \partial_{\tilde{x}}^2 + \partial_{\tilde{y}}^2$ is the horizontal Laplacian, $J(f, g) \stackrel{\text{def}}{=} (\partial_{\tilde{x}}f)(\partial_{\tilde{y}}g) - (\partial_{\tilde{y}}f)(\partial_{\tilde{x}}g)$ is the Jacobian, $\tilde{\Delta}_{\lambda} \stackrel{\text{def}}{=} \tilde{\Delta} - 2\tilde{\lambda}^2$, $\tilde{\zeta} \stackrel{\text{def}}{=} \tilde{\Delta}\tilde{\psi}$ is the barotropic vorticity, $\tilde{\eta} \stackrel{\text{def}}{=} \tilde{\Delta}_{\lambda}\tilde{\psi}$, \tilde{x} and \tilde{y} are the coordinates in the zonal and the meridional direction respectively and the tilde denotes dimensional quantities (cf. Cehelsky & Tung (1991)). The deformation radius is $1/\tilde{\lambda} = \sqrt{g'(H/2)/f_0}$, where $g' = 2g(\rho_1 - \rho_2)/(\rho_1 + \rho_2)$ is the reduced gravity and f_0 is the Coriolis parameter at the center of the plane, $\tilde{\beta}$ is the planetary vorticity gradient and \tilde{r} is the coefficient of linear damping of potential vorticity.

We do not impose a temperature gradient across the channel, which through thermal wind balance would impose a mean baroclinic shear. Instead of this large scale forcing, we impose random baroclinic and barotropic potential vorticity sources and sinks, denoted $\tilde{\xi}^{\psi}$ and $\tilde{\xi}^{\theta}$ respectively. These sources and sinks represent barotropic and baroclinic excitation of the fluid by sub-scale processes or by processes not included in the quasi-geostrophic dynamics such as convection. The random excitation is assumed to have zero mean, to be temporally delta correlated and to be statistically homogeneous in the horizontal. Under these assumptions, the excitations in the upper layer, $\tilde{\xi}_1(\tilde{x}, \tilde{t})$, and in the lower layer, $\tilde{\xi}_2(\tilde{x}, \tilde{t})$, have the two-point, two-time covariances:

$$\langle \tilde{\xi}_i(\tilde{x}_a, \tilde{t}_a) \tilde{\xi}_j(\tilde{x}_b, \tilde{t}_b) \rangle = \langle \tilde{\xi}_j(\tilde{x}_a, \tilde{t}_a) \tilde{\xi}_i(\tilde{x}_b, \tilde{t}_b) \rangle = \delta(\tilde{t}_a - \tilde{t}_b) \tilde{\alpha}_{ij}(\tilde{x}_a - \tilde{x}_b), \quad i, j = 1, 2, \quad (2.3)$$

where $\langle \cdot \rangle$ denotes an ensemble average over forcing realizations, $\tilde{x} = (\tilde{x}, \tilde{y})$, and the subscript denotes two different points a and b . Statistical homogeneity requires that the covariances are symmetric to the exchange of points a and b and to the exchange of the

excitation of the two layers. Therefore the functions $\tilde{\alpha}_{ij}$ satisfy:

$$\tilde{\alpha}_{11} = \tilde{\alpha}_{22} = 2\tilde{\Xi} \quad , \quad \tilde{\alpha}_{12} = \tilde{\alpha}_{21} = 2\tilde{\Xi}_{12} \quad . \quad (2.4)$$

An important consequence of this symmetry is that the baroclinic and barotropic components of the excitation

$$\tilde{\xi}^\psi = \frac{\tilde{\xi}_1 + \tilde{\xi}_2}{2} \quad , \quad \tilde{\xi}^\theta = \frac{\tilde{\xi}_1 - \tilde{\xi}_2}{2} \quad , \quad (2.5)$$

are uncorrelated:

$$\langle \tilde{\xi}^\psi(\tilde{\mathbf{x}}_a, \tilde{t}_a) \tilde{\xi}^\theta(\tilde{\mathbf{x}}_b, \tilde{t}_b) \rangle = 0. \quad (2.6)$$

The barotropic and baroclinic component covariances of the forcing are:

$$\langle \tilde{\xi}^\psi(\tilde{\mathbf{x}}_a, \tilde{t}_a) \tilde{\xi}^\psi(\tilde{\mathbf{x}}_b, \tilde{t}_b) \rangle = \delta(\tilde{t}_a - \tilde{t}_b) \left[\tilde{\Xi}(\tilde{\mathbf{x}}_a - \tilde{\mathbf{x}}_b) + \tilde{\Xi}_{12}(\tilde{\mathbf{x}}_a - \tilde{\mathbf{x}}_b) \right] \quad , \quad (2.7)$$

$$\langle \tilde{\xi}^\theta(\tilde{\mathbf{x}}_a, \tilde{t}_a) \tilde{\xi}^\theta(\tilde{\mathbf{x}}_b, \tilde{t}_b) \rangle = \delta(\tilde{t}_a - \tilde{t}_b) \left[\tilde{\Xi}(\tilde{\mathbf{x}}_a - \tilde{\mathbf{x}}_b) - \tilde{\Xi}_{12}(\tilde{\mathbf{x}}_a - \tilde{\mathbf{x}}_b) \right] \quad . \quad (2.8)$$

If we assume a correlation between the layers $\tilde{\Xi}_{12} = p\tilde{\Xi}$, positive definiteness of the covariances implies that $|p| \leq 1$. We consider three values for p that span this range and exemplify opposite limits. We consider the value $p = 1$ which corresponds to the case of imposing the same excitation on the two layers ($\tilde{\xi}_1 = \tilde{\xi}_2$). For this forcing, the baroclinic forcing covariance is zero and represents at first sight the worst (best) case scenario for the emergence of mean flows with strong baroclinic (barotropic) components. In the second case we take the opposite limit of exciting only the baroclinic part of the flow ($p = -1$) by imposing an anti-correlated excitation in the two layers ($\tilde{\xi}_2 = -\tilde{\xi}_1$). This represents the best (worst) case scenario for the emergence of mean flows with strong baroclinic (barotropic) components. Finally we take $p = 0$ and consider an independent excitation of the two layers $\tilde{\Xi}_{12} = 0$. In that case, the barotropic and baroclinic forcing covariances are equal:

$$\langle \tilde{\xi}^\psi(\tilde{\mathbf{x}}_a, \tilde{t}_a) \tilde{\xi}^\psi(\tilde{\mathbf{x}}_b, \tilde{t}_b) \rangle = \langle \tilde{\xi}^\theta(\tilde{\mathbf{x}}_a, \tilde{t}_a) \tilde{\xi}^\theta(\tilde{\mathbf{x}}_b, \tilde{t}_b) \rangle = \delta(\tilde{t}_a - \tilde{t}_b) \tilde{\Xi}(\tilde{\mathbf{x}}_a - \tilde{\mathbf{x}}_b) \quad . \quad (2.9)$$

In this work we address the following questions:

- a) For a given spatial structure of the homogeneous forcing Ξ , do any coherent structures with scales different than the ones we directly excite emerge in the flow and what are their characteristics? We are particularly interested in whether the structures that appear are baroclinic or necessarily barotropic.
- b) Can we develop a theory that is able to explain the emergence of coherent structures and predict their characteristics?

To address the first question, we consider (2.1)-(2.2) in a doubly periodic channel of size $2\pi \times 2\pi$ and integrate the equations using a pseudo-spectral code and a fourth-order Runge-Kutta time stepping scheme. For the spatial structure of the excitation, we assume that the forcing injects energy in a thin ring in wavenumber space that has radius \tilde{k}_f and width $\Delta\tilde{k}_f$ (Lilly 1969). The power spectrum of the spatial covariance of the forcing is therefore:

$$\hat{\Xi}(\tilde{\mathbf{k}}) = \sum_{\tilde{k}_x} \sum_{\tilde{k}_y} \tilde{\Xi}(\tilde{\mathbf{x}}_a - \tilde{\mathbf{x}}_b) e^{-i\tilde{\mathbf{k}} \cdot (\tilde{\mathbf{x}}_a - \tilde{\mathbf{x}}_b)} = \begin{cases} a_f, & \text{for } |\tilde{k} - \tilde{k}_f| \leq \Delta\tilde{k}_f \\ 0, & \text{for } |\tilde{k} - \tilde{k}_f| > \Delta\tilde{k}_f \end{cases} \quad , \quad (2.10)$$

where $\tilde{\mathbf{k}} = (\tilde{k}_x, \tilde{k}_y)$ is the wavevector with total wavenumber $\tilde{k} = |\tilde{\mathbf{k}}|$ and \tilde{k}_x, \tilde{k}_y assume

integer values. The amplitude

$$a_f = \frac{\tilde{\varepsilon} \tilde{k}^2 (\tilde{k}^2 + 2\tilde{\lambda}^2)^2}{4(\tilde{k}^4 + (2+p)\tilde{\lambda}^4 + 3\tilde{k}^2\tilde{\lambda}^2)\Delta\tilde{k}_f}, \quad (2.11)$$

is chosen so that the forcing injects energy at a rate $\tilde{\varepsilon}$ in the flow.

We use the modest $M = 32 \times 32$ resolution and the rather low value $\tilde{k}_f = 6$ ($\Delta\tilde{k}_f = 1$). The reason is that we would like to explain the phenomena observed in the direct numerical simulations denoted as NL, with the statistical theory to be developed in sections 3-5 that requires the integration of the highly dimensional covariance matrix (for a grid with M points the covariance has dimension $2M^2$). However, the low resolution results were compared to higher resolution simulations and there were no significant differences found. In one layer flows with the present geometry strong and persistent large scale flows were produced when the non-dimensional planetary vorticity gradient $\beta = \tilde{\beta}/\tilde{k}_f\tilde{r}$ is large (Bakas & Ioannou 2014). Taking into consideration these results we chose $\tilde{\beta} = 60$ and $\tilde{r} = 0.1$ yielding the non-dimensional value of $\beta = 100$, which also roughly corresponds to that in the Jovian atmosphere.

Previous studies on the emergence of large scale structures in forced-dissipative turbulence have used two indices to quantify the energy in the emerging large scale structures. The first is the zonal mean flow (zmf) index

$$\text{zmf} = \frac{\sum_{\tilde{k}_y: \tilde{k}_y < \tilde{k}_f - \Delta\tilde{k}_f} \hat{E}(\tilde{k}_x = 0, \tilde{k}_y)}{\sum_{\tilde{k}_x \tilde{k}_y} \hat{E}(\tilde{k}_x, \tilde{k}_y)}, \quad (2.12)$$

with

$$\hat{E}(\tilde{k}_x, \tilde{k}_y) = \lim_{T \rightarrow \infty} \frac{1}{T} \int_0^T \tilde{k}^2 \left(|\hat{\psi}|^2 + |\hat{\theta}|^2 \right) d\tilde{t}, \quad (2.13)$$

the time averaged kinetic energy of the flow at wavenumbers $(\tilde{k}_x, \tilde{k}_y)$. The zmf index determines the ratio of the energy of the zonal component of the flow ($\tilde{k}_x = 0$) to the energy of the perturbation field and was used by Srinivasan & Young (2012) to study the emergence of jets in barotropic turbulence. The second is the non-zonal mean flow (nzmf) index:

$$\text{nzmf} = \frac{\sum_{\tilde{k}_x \tilde{k}_y: \tilde{k} < \tilde{k}_f - \Delta\tilde{k}_f} \hat{E}(\tilde{k}_x \neq 0, \tilde{k}_y)}{\sum_{\tilde{k}_x \tilde{k}_y} \hat{E}(\tilde{k}_x, \tilde{k}_y)}, \quad (2.14)$$

that measures the energy in waves with scales larger than the scale of the forcing ($\tilde{k} < \tilde{k}_f$) and was used by Bakas & Ioannou (2013a) to study the emergence of large scale waves. If the large scale structures that emerge are coherent, then these indices quantify their amplitude.

Figure 1 shows the dependence of the nzmf and zmf indices on the energy input rate $\tilde{\varepsilon}$ for NL simulations with a Rossby radius of deformation comparable to the forcing scale $\tilde{\lambda} = \tilde{k}_f$ and an uncorrelated forcing between the two layers ($p = 0$). We observe that for $\tilde{\varepsilon}$ lower than the critical value $\tilde{\varepsilon}_c$, which will be theoretically predicted in section 4, there are no large scale structures in the flow. This can also be verified by the kinetic energy power spectra shown in figure 2a-b, as the spectra contain only the ring of forced wavenumbers with little energy spill-over to other scales for the baroclinic part of the flow. Therefore the flow is dominated by the directly forced waves shown in figure 2c that obey the Rossby wave dispersion but are phase incoherent. To quantify this we calculate the ensemble mean of the frequency power spectrum of the streamfunction field

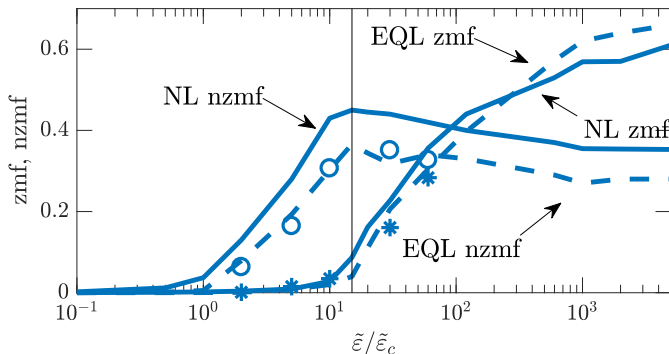


FIGURE 1. The zmf and nzm indices defined in (2.12) and (2.14) respectively, as a function of the energy input rate $\tilde{\epsilon}$ for the fully nonlinear (NL) integrations (solid lines), the ensemble quasi-linear (EQL) integrations (dashed lines) and the S3T simulations (open circles for the nzm and stars for the zmf index). The later two are discussed in sections 5-6. The critical energy input rate $\tilde{\epsilon}_c$ for which the homogeneous state becomes unstable is calculated from the S3T stability analysis (in section 4) and the critical energy input rate $\tilde{\epsilon}_{nl}$ for which the traveling wave states become unstable with respect to zonal perturbations is shown by the vertical thin line (see section 5). The parameters values are $\tilde{\beta} = 60$, $\tilde{k}_f = 6$, $\Delta\tilde{k}_f = 1$, $\tilde{r} = 0.1$, $\tilde{\lambda} = \tilde{k}_f$ and the forcing between the two layers is uncorrelated ($p = 0$).

at wavenumber $(\tilde{k}_x, \tilde{k}_y)$:

$$\psi_{cor} = \left\langle |\hat{\psi}(\tilde{k}_x, \tilde{k}_y, \tilde{\omega})|^2 \right\rangle, \quad (2.15)$$

where

$$\hat{\psi}(\tilde{k}_x, \tilde{k}_y, \tilde{\omega}) = \int \sum_{\tilde{x}, \tilde{y}} \psi(\tilde{x}, \tilde{y}, \tilde{t}) e^{-i\tilde{k} \cdot \tilde{x} - i\tilde{\omega} \tilde{t}} d\tilde{t}, \quad (2.16)$$

for the barotropic component of the flow. Similarly we calculate θ_{cor} for the baroclinic part. Travelling waves manifest as peaks at specific frequencies with phase coherence over times proportional to the inverse of the half-width of their resonant peak. We consider that the structure that emerges in the NL is phase coherent when its coherence time exceeds the dissipation time scale, which is the time over which a linear wave stochastically excited by white noise remains coherent. Figure 2d shows the barotropic frequency power spectrum ψ_{cor} normalized to unit maximum amplitude for one of the waves in the forced ring with wavenumbers $(\tilde{k}_{xr}, \tilde{k}_{yr}) = (1, 5)$. The frequency power spectrum peaks at the Rossby wave frequency $\omega_r = \tilde{\beta}\tilde{k}_{xr}/(\tilde{k}_{xr}^2 + \tilde{k}_{yr}^2)$, while comparison of its half-width with the corresponding half-width of the power spectrum of stochastically forced linear Rossby waves with the same wavenumbers shows that the coherence time for these waves is the dissipation time scale.

The rapid increase in the nzm index for $\tilde{\epsilon} > \tilde{\epsilon}_c$ shown in figure 1, signifies the emergence of large scale waves in the flow. The scales of the waves are shown in figure 3 which illustrates the kinetic energy power spectra of the NL simulations for $\tilde{\epsilon} = 2\tilde{\epsilon}_c$. We observe that the kinetic energy of the barotropic part of the flow (cf. figure 3a) peaks at wavenumbers $(|\tilde{k}_x|, |\tilde{k}_y|) = (1, 4)$ and $(|\tilde{k}_x|, |\tilde{k}_y|) = (2, 4)$. In Figure 3c we plot the barotropic frequency power spectrum ψ_{cor} for the two $\tilde{\mathbf{k}} = (1, 4)$ and $\tilde{\mathbf{k}} = (2, 4)$ dominant barotropic structures and compare them with the corresponding power spectrum of stochastically forced linear Rossby waves with the same wavenumbers. We observe that both the $(1, 4)$ and the $(2, 4)$ waves remain phase coherent (over six and two dissipation time scales respectively) and also satisfy to a good approximation the Rossby wave dispersion

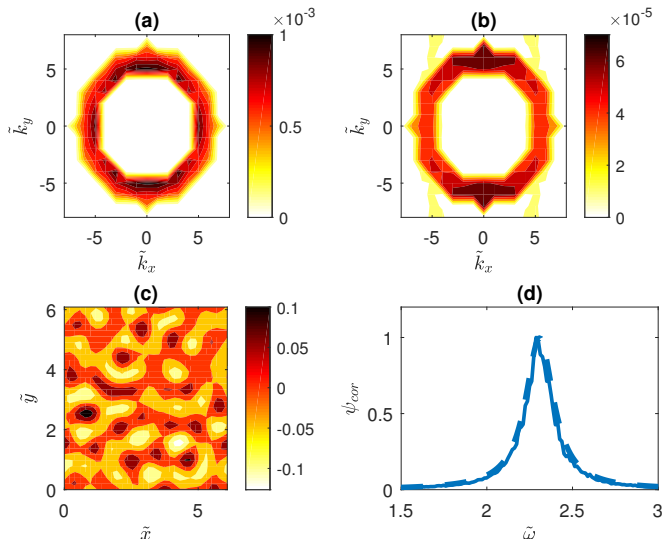


FIGURE 2. (a)-(b) Long time average of the kinetic energy power spectra of the (a) barotropic and (b) baroclinic part of the turbulent flow at statistical equilibrium obtained from an NL simulation at $\tilde{\varepsilon} = \tilde{\varepsilon}_c/2$. (c) Snapshot of the barotropic streamfunction at statistical equilibrium. (d) The ensemble mean frequency power spectrum ψ_{cor} (defined in (2.15)) for the $\tilde{\mathbf{k}} = (1, 5)$ non-zonal barotropic structure. The frequency power spectrum is normalized to unit maximum amplitude for illustration purposes. The corresponding normalized ψ_{cor} for linear Rossby waves with the same wavenumber and stochastically forced by white noise is also shown (dashed lines) for comparison. The rest of the parameter values are the same as in figure 1.

as ψ_{cor} peaks at the corresponding Rossby wave frequencies for both wavenumbers. In contrast, the baroclinic component of the flow is very weak compared to the barotropic part (cf. figure 3b) and the emergent structures have an incoherent baroclinic part. For example, the wave with $\tilde{\mathbf{k}} = (4, 0)$ that achieves maximum kinetic energy for the baroclinic component remains phase coherent for very short times (shorter than $1/\tilde{\tau}$) as revealed by its frequency power spectrum θ_{cor} that is shown in figure 3d. We can therefore conclude that large scale, phase coherent, barotropic Rossby waves emerge in the flow for $\tilde{\varepsilon} > \tilde{\varepsilon}_c$. For larger energy input rates the energy in these large scale waves increases (increasing nzmf index in figure 1) as well as the scales of the dominant waves.

When the energy input rate passes a second threshold $\tilde{\varepsilon}_{nl}$, which will be calculated in section 5, large scale zonal jets emerge as signified by the increase of the zmf index for $\tilde{\varepsilon} > \tilde{\varepsilon}_{nl}$ shown in figure 1. The barotropic kinetic energy spectra for $\tilde{\varepsilon} = 60\tilde{\varepsilon}_c$ shown in figure 4a, reveal that the zonal jet with $(|\tilde{k}_x|, |\tilde{k}_y|) = (0, 2)$ dominates the flow, while there is a secondary peak at the wave with $(|\tilde{k}_x|, |\tilde{k}_y|) = (1, 3)$ that is phase coherent (not shown). The baroclinic part of the spectrum is isotropic and fills the whole area inside the ring of forced wavenumbers but is five orders of magnitude smaller. As the energy input rate further increases the energy being pumped into the barotropic zonal jets increases, while the energy of the large scale barotropic waves decreases (cf. figure 1; The scales of both the jets and the waves also increase. In summary, there are two regime transitions in the flow as the energy input rate of the forcing increases. In the first transition, phase coherent, large scale Rossby waves emerge and break the homogeneity of the turbulent flow and in the second transition large scale barotropic zonal jets emerge.

For lower values of the Rossby radius of deformation $\tilde{\lambda}$, the bifurcation diagram is

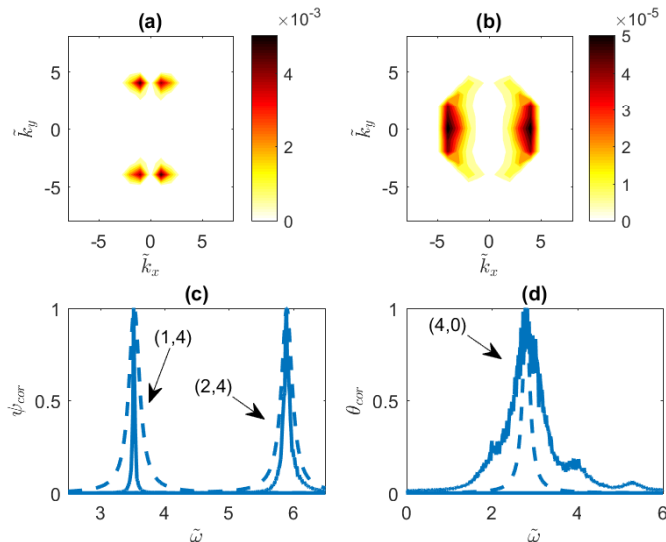


FIGURE 3. (a)-(b) Long time average of the kinetic energy power spectra of the (a) barotropic and (b) baroclinic part of the turbulent flow at statistical equilibrium, obtained from an NL simulation at $\tilde{\varepsilon} = 2\tilde{\varepsilon}_c$. Shown are the spectra in the region in wavenumber space inside the forced ring. (c) The ensemble mean frequency power spectrum ψ_{cor} for the two $\tilde{\mathbf{k}} = (1, 4)$ and $\tilde{\mathbf{k}} = (2, 4)$ non-zonal barotropic structures dominating the kinetic energy power spectra in (a). The frequency power spectrum is normalized to unit maximum amplitude for illustration purposes (as observed in (a) the $\tilde{\mathbf{k}} = (1, 4)$ structure has about twice the energy of the $\tilde{\mathbf{k}} = (2, 4)$ structure). (d) The ensemble mean frequency power spectrum θ_{cor} for the $\tilde{\mathbf{k}} = (4, 0)$ non-zonal baroclinic structure dominating the kinetic energy power spectra in (b). In (c) and (d) the corresponding normalized ψ_{cor} and θ_{cor} for linear Rossby waves with the same wavenumbers and stochastically forced by white noise is also shown (dashed lines) for comparison. The rest of the parameter values are the same as in figure 1.

similar with the two regimes of large scale waves and large scale jets evident when the energy input rate passes a critical value. However, the structures that dominate the flow have a baroclinic component as well. Figure 5 shows the kinetic energy power spectra for $\tilde{\lambda} = \tilde{k}_f/6$ and two values of the energy input rate above the critical threshold $\tilde{\varepsilon}_c$. For low energy input rates (c.f. figure 5a,b), the flow is dominated by a barotropic wave with $(|\tilde{k}_x|, |\tilde{k}_y|) = (1, 4)$ and a baroclinic wave with $(|\tilde{k}_x|, |\tilde{k}_y|) = (1, 3)$ and an amplitude for the baroclinic streamfunction about half of the amplitude of the barotropic streamfunction. Calculation of the frequency power spectra ψ_{cor} and θ_{cor} reveals that both of these waves follow the Rossby wave dispersion and remain phase coherent over times longer than the dissipation time scale (not shown).

At larger energy input rates (c.f. figure 5c,d), the flow is dominated by a barotropic jet accompanied by a baroclinic wave. This state was found to exhibit significant variability at long time scales of the order of $10/\tilde{r}$. Figure 6a shows the evolution of the zmf and nzmf indices. We observe a low frequency variability of the two indices that are anti-correlated, with time periods of stronger jets/weaker waves and time periods of weaker jets/stronger waves. Similar variability is observed in the baroclinicity measure:

$$R_b = \frac{\sum_{\tilde{k}_x, \tilde{k}_y} (\tilde{k}^2 + 2\tilde{\lambda}^2) |\hat{\theta}(\tilde{\mathbf{k}})|^2}{\sum_{\tilde{k}_x, \tilde{k}_y} \tilde{k}^2 |\hat{\psi}(\tilde{\mathbf{k}})|^2}, \quad (2.17)$$

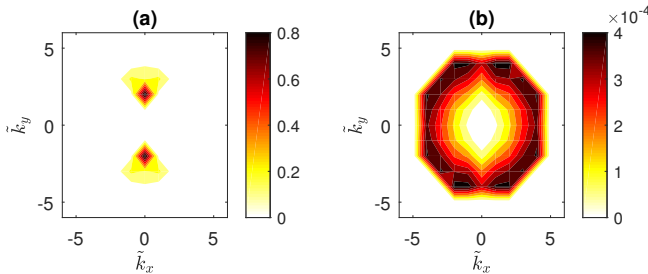


FIGURE 4. Long time average of the kinetic energy power spectra of the (a) barotropic and (b) baroclinic part of the turbulent flow at statistical equilibrium obtained for a NL simulation with $\tilde{\varepsilon} = 60\tilde{\varepsilon}_c$. The rest of the parameter values are the same as in figure 1.

that is shown in figure 6b, where the periods of stronger waves are accompanied by higher values for the flow baroclinicity. Therefore, we observe an energy exchange between the barotropic zonal jet and the large scale baroclinic wave. For larger energy input rates, the baroclinic part of the flow weakens along with the amplitude of this low frequency variability. As a result, for geophysical flows that are highly supercritical with respect to the structure forming instability such as the Jovian atmosphere, the baroclinic component of the flow is expected to be very weak.

We now test the sensitivity of the obtained results to the forcing correlation between the two layers. The barotropic forcing ($p = 1$) presents at first sight the worst case scenario for symmetry breaking by baroclinic structures since only barotropic eddies are injected in the flow. However, the regime transitions observed for uncorrelated forcing remain the same. That is, when $\tilde{\lambda} = \tilde{k}_f$ barotropic structures break the homogeneity of the turbulent flow when the energy input rate passes a critical threshold. When the energy is injected at scales smaller than the Rossby radius of deformation ($\tilde{\lambda} = \tilde{k}_f/6$) both barotropic and baroclinic large scale, phase coherent waves emerge in the flow. For higher energy input rates, the flow gets zonated and barotropized. Therefore, the regime transitions in this case are not shown.

In contrast, the baroclinic forcing ($p = -1$) presents at first sight the worst case scenario for the emergence of barotropic flows. For $\tilde{\lambda} = \tilde{k}_f/6$ the regime transitions are the same as in the case of uncorrelated forcing ($p = 0$) and are not shown. The case of $\tilde{\lambda} = \tilde{k}_f$ is shown in figure 7. For energy input rates below a critical threshold the flow remains homogeneous. As shown in figure 7a, the kinetic energy power spectrum of the baroclinic component shows significant power only in the directly forced ring of wavenumbers, while the power spectrum of the barotropic part of the flow is more than two orders of magnitude smaller and is not shown. This is no surprise since we inject only baroclinic eddies in the flow. When the energy input rate passes a critical threshold, barotropic waves emerge in the flow with scales comparable to the forcing scale \tilde{k}_f even though we do not directly force

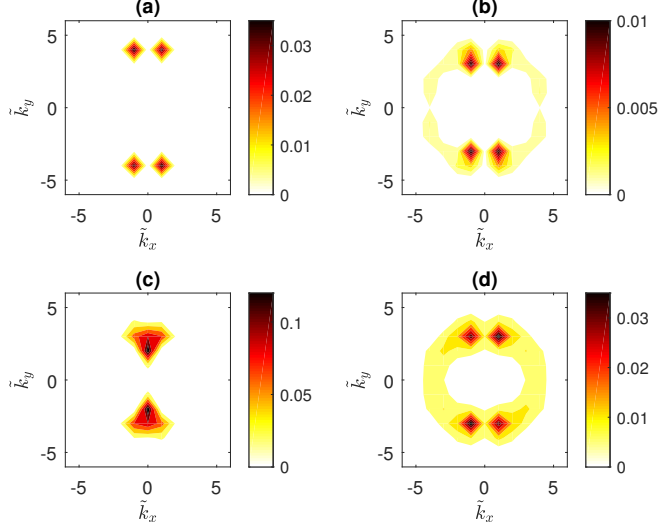


FIGURE 5. (a)-(b) Long-time average of the kinetic energy power spectra of the (a) barotropic and (b) baroclinic part of the turbulent flow at statistical equilibrium for a NL simulation with $\tilde{\varepsilon} = 10\tilde{\varepsilon}_c$. (c)-(d) The same as (a)-(b) but for $\tilde{\varepsilon} = 40\tilde{\varepsilon}_c$. The deformation radius is $\tilde{\lambda} = \tilde{k}_f/6$ and the rest of the parameter values are the same as in figure 1.

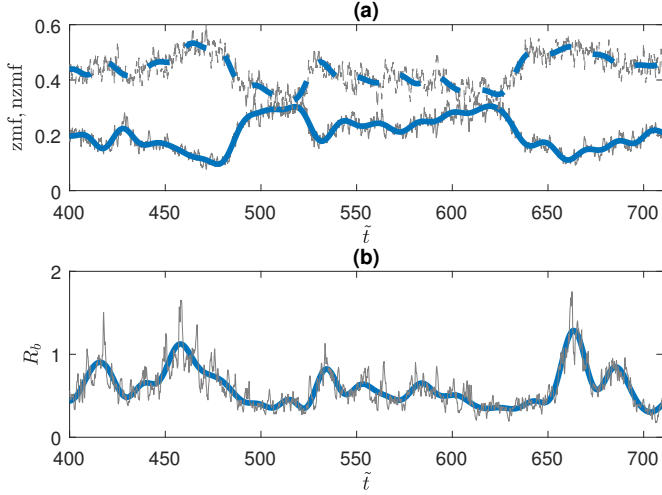


FIGURE 6. (a) Evolution of the zmf (solid) and nzmf (dashed) indices (thin lines). The thick lines show the low pass filtered time series of the indices. (b) Evolution of the baroclinicity ratio (thin line). The thick line shows a low pass filtered time series of R_b . The energy input rate is $\tilde{\varepsilon} = 40\tilde{\varepsilon}_c$, the deformation radius is $\tilde{\lambda} = \tilde{k}_f/6$ and the rest of the parameters are as in figure 1.

barotropic eddies. This is revealed by the kinetic energy power spectrum of the barotropic part of the flow that is shown for $\tilde{\varepsilon} = 4\tilde{\varepsilon}_c$ in figure 7b and peaks at $(|\tilde{k}_x|, |\tilde{k}_y|) = (1, 6)$. The correlation power spectrum of this dominant wave that is shown in figure 7c reveals that these are phase coherent waves. For larger input rates ($\tilde{\varepsilon} = 60\tilde{\varepsilon}_c$) shown in figure 7, the coherent part of the flow is zoned as in all cases previously discussed.

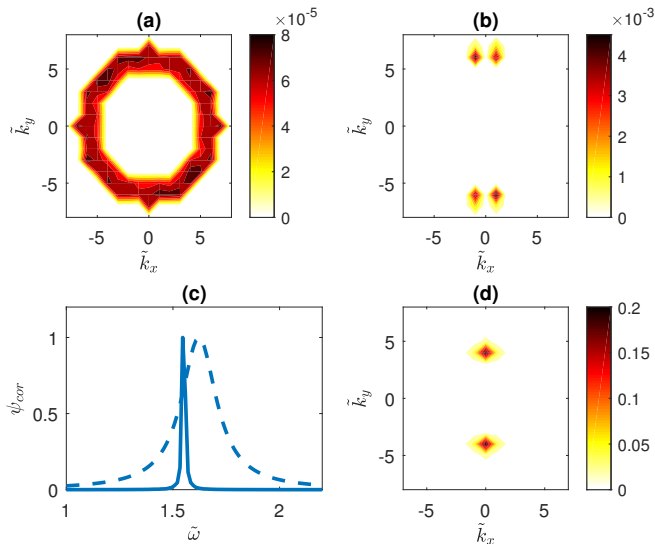


FIGURE 7. (a) Long time average of the kinetic energy power spectra of the baroclinic part of the turbulent flow at statistical equilibrium for $\tilde{\varepsilon} = \tilde{\varepsilon}_c/2$. (b) Long time average of the kinetic energy power spectra of the barotropic part of the flow for $\tilde{\varepsilon} = 4\tilde{\varepsilon}_c$. (c) The ensemble mean frequency power spectrum ψ_{cor} for the $\tilde{\mathbf{k}} = (1, 6)$ barotropic wave dominating the power spectra in (b). (d) Long time average of the kinetic energy power spectra of the barotropic part of the flow for $\tilde{\varepsilon} = 60\tilde{\varepsilon}_c$. The forcing is baroclinic ($p = -1$), $\tilde{\lambda} = \tilde{k}_f$ and the rest of the parameter values are the same as in figure 1. These simulations were performed with a 64×64 resolution.

A slightly different picture emerges when energy is injected at scales larger than the deformation radius as the wave regime is absent. For example, when $\tilde{\lambda} = 2\tilde{k}_f$ there is only one regime transition in the turbulent flow as the energy input rate of the forcing is increased with the emergence of zonal jets breaking the translational symmetry in the flow. Figure 8 illustrates the kinetic energy power spectrum of the barotropic part for two supercritical values of the energy input rate. For low energy input rates shown in figure 8a ($\tilde{\varepsilon} = 4\tilde{\varepsilon}_c$), the jets have scales comparable to the deformation scale as the power spectra peak at $|\tilde{k}_y| = 3\tilde{\lambda}/4$. For larger energy input rates shown in figure 8b the jets obtain larger scales and as the energy input rate is further increased the energy is pumped into larger and larger scale jets.

To summarize, when the energy injection scale is comparable to the Rossby radius of deformation, the homogeneity of the flow is broken by the emergence of large scale barotropic waves and large scale zonal jets when the energy input rate passes certain thresholds. When the energy injection scale is smaller than the Rossby radius of deformation, both barotropic and baroclinic large scale waves emerge in the flow and for large energy input rates the barotropic part of the flow is zonated and becomes dominant. These results are in general independent of the correlation of the excitation between the two layers with minor exceptions (for example the absence of the wave regime when the energy injection scale is larger than the Rossby radius of deformation). In the following sections we develop a theory that explains the emergence of large scale flows as a bifurcation in the turbulent flow and is also able to predict the characteristics and amplitudes of the emergent structures.

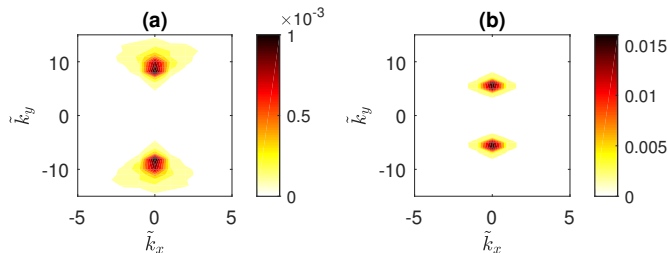


FIGURE 8. Long time average of the kinetic energy power spectra of the barotropic part of the turbulent flow at statistical equilibrium for (a) $\tilde{\varepsilon} = 4\tilde{\varepsilon}_c/2$ and (b) $\tilde{\varepsilon} = 60\tilde{\varepsilon}_c$. The forcing is baroclinic ($p = -1$), $\tilde{\lambda} = 2\tilde{k}_f$ and the rest of the parameter values are the same as in figure 1. These simulations were performed with a 64×64 resolution.

3. Stochastic Structural Stability Theory

In order to analyze the transition from a statistically homogeneous to a statistically inhomogeneous turbulent state, we consider the Statistical State Dynamics (SSD) of the two-layer model (2.1)-(2.2) which comprises the dynamics of the cumulants of the flow. Due to the infinite hierarchy of the resulting equations, this system has to be closed at a certain order through an approximation or assumption. We follow previous studies and consider a second order closure that is called S3T or CE2 (Farrell & Ioannou 2003; Marston *et al.* 2008). The cumulants are defined by using a proper averaging operator (cf. Monin & Yaglom (1973)) that captures the emergent large-scale structure (e.g., zonal jet or planetary-scale wave) and additionally satisfies the ergodic property that the second-order cumulants are equal to the ensemble average over forcing realizations under the same first cumulant. In order to address the emergence of both zonal jets and coherent waves in this work, we employ the ensemble average and interpret it as an average over an intermediate time scale which is long compared to the time scale of the evolution of the incoherent flow but short compared to the time scale for the evolution of the mean. Similar assumptions for the average separating fast from slow motions or large scale from small scale motions were also made in previous studies (Bernstein & Farrell 2010; Bakas & Ioannou 2014; Marston *et al.* 2016; Constantinou *et al.* 2016; Bouchet *et al.* 2018).

In order to formulate the theory for the two-layer flow, we first non-dimensionalize (2.1)-(2.2) by choosing the damping relaxation time scale, $1/\tilde{r}$, as the characteristic time scale and the scale of the excitation, $1/\tilde{k}_f$, as the characteristic length scale. The non-dimensional variables are: $[\zeta, \eta] = [\tilde{\zeta}, \tilde{\eta}]/\tilde{r}$, $[\psi, \theta] = [\tilde{\psi}, \tilde{\theta}]\tilde{k}_f^2/\tilde{r}$, $[\xi^\psi, \xi^\theta] = [\tilde{\xi}^\psi, \tilde{\xi}^\theta]/\tilde{r}^2$, $\varepsilon = \tilde{\varepsilon}\tilde{k}_f^2/\tilde{r}^3$, $\beta = \tilde{\beta}/(\tilde{k}_f\tilde{r})$, $\lambda = \tilde{\lambda}/\tilde{k}_f$ and $r = 1$. Thus, the non-dimensional version of (2.1)-(2.2) lacks all tildes and has $r = 1$. We also approximate the ring forcing spectrum (2.10) with a forcing covariance that is isotropic and injects energy in a delta-ring in

wavenumber space of radius 1:

$$\hat{\Xi}(\mathbf{k}) = \frac{\varepsilon(1 + 2\lambda^2)^2}{2(1 + (2 + p)\lambda^4 + 3\lambda^2)} \delta(k - 1) . \quad (3.1)$$

Again, the amplitude is chosen to yield an energy injection rate ε .

The first cumulant of the barotropic and baroclinic streamfunctions are $\Psi(\mathbf{x}, t) \stackrel{\text{def}}{=} \langle \psi \rangle$ and $\Theta(\mathbf{x}, t) \stackrel{\text{def}}{=} \langle \theta \rangle$, while the eddy field is denoted with dashes and defined as $\psi'(\mathbf{x}, t) = \psi - \langle \psi \rangle$, $\theta'(\mathbf{x}, t) \stackrel{\text{def}}{=} \theta - \langle \theta \rangle$. In order to derive the S3T system we first derive from (2.1)-(2.2) the equations for the mean and the eddies:

$$\partial_t Z + J(\Psi, Z) + J(\Theta, \Delta\Theta) + \beta \partial_x \Psi = -\langle J(\psi', \zeta') + J(\theta', \Delta\theta') \rangle - Z , \quad (3.2)$$

$$\partial_t H + J(\Psi, H) + J(\Theta, Z) + \beta \partial_x \Theta = -\langle J(\psi', \eta') + J(\theta', \zeta') \rangle - H , \quad (3.3)$$

$$\begin{aligned} \partial_t \zeta' + J(\Psi, \zeta') + J(\psi', Z) + J(\Theta, \Delta\theta') + J(\theta', \Delta\Theta) + \beta \partial_x \psi' = \\ = \underbrace{\langle J(\psi', \zeta') + J(\theta', \Delta\theta') \rangle}_{N_\psi} - \left(J(\psi', \zeta') + J(\theta', \Delta\theta') \right) - \zeta' + \xi^\psi , \end{aligned} \quad (3.4)$$

$$\begin{aligned} \partial_t \eta' + J(\Psi, \eta') + J(\psi', H) + J(\Theta, \zeta') + J(\theta', Z) + \beta \partial_x \theta' = \\ = \underbrace{\langle J(\psi', \eta') + J(\theta', \zeta') \rangle}_{N_\theta} - \left(J(\psi', \eta') + J(\theta', \zeta') \right) - \eta' + \xi^\theta . \end{aligned} \quad (3.5)$$

Neglecting the eddy-eddy nonlinear terms N_ψ and N_θ in (3.4)-(3.5), we can obtain the quasi-linear approximation for the eddies:

$$\partial_t [\zeta', \eta']^T = \mathbf{A}[\zeta', \eta']^T + [\xi^\psi, \xi^\theta]^T , \quad (3.6)$$

where

$$\mathbf{A} \stackrel{\text{def}}{=} \begin{pmatrix} \left(\Delta U^\psi \Delta^{-1} - U^\psi \right) \cdot \nabla - \beta \partial_x \Delta^{-1} - 1 & -U^\theta \cdot \nabla \Delta \Delta_\lambda^{-1} + \Delta U^\theta \cdot \nabla \Delta_\lambda^{-1} \\ -U^\theta \cdot \nabla + \Delta_\lambda U^\theta \cdot \nabla \Delta^{-1} & \left(\Delta U^\psi \Delta_\lambda^{-1} - U^\psi \right) \cdot \nabla - \beta \partial_x \Delta_\lambda^{-1} - 1 \end{pmatrix} , \quad (3.7)$$

is the linear operator governing the evolution of the eddies about the instantaneous mean flow $[U^\psi, U^\theta]^T$, T denotes the matrix transpose and Δ^{-1} , Δ_λ^{-1} are the integral operators that invert ζ' and η' into the barotropic and baroclinic streamfunction fields. Equations (3.2)-(3.3) and (3.6) constitute the ensemble quasi-linear (EQL) approximation to the fully non-linear dynamics.

The S3T system is then obtained by first expressing the eddy fluxes forcing the barotropic and baroclinic flow in terms of the second cumulant

$$\mathbf{C}(\mathbf{x}_a, \mathbf{x}_b) \stackrel{\text{def}}{=} \mathbf{C}_{ab} = \begin{pmatrix} \langle \zeta'_a \zeta'_b \rangle & \langle \zeta'_a \eta'_b \rangle \\ \langle \eta'_a \zeta'_b \rangle & \langle \eta'_a \eta'_b \rangle \end{pmatrix} = \begin{pmatrix} C_{ab}^{\zeta\zeta} & C_{ab}^{\zeta\eta} \\ C_{ab}^{\eta\zeta} & C_{ab}^{\eta\eta} \end{pmatrix} , \quad (3.8)$$

that is the covariance matrix of the eddy fields ζ' , η' . In (3.8) we use the shorthand $\zeta'_a = \zeta'(\mathbf{x}_a, t)$, to refer to the value of the relative barotropic vorticity at the specific point \mathbf{x}_a (and similarly for η'). Defining the streamfunction covariance matrix

$$\mathbf{S}(\mathbf{x}_a, \mathbf{x}_b) \stackrel{\text{def}}{=} \mathbf{S}_{ab} = \begin{pmatrix} S_{ab}^{\psi\psi} & S_{ab}^{\psi\theta} \\ S_{ab}^{\theta\psi} & S_{ab}^{\theta\theta} \end{pmatrix} , \quad (3.9)$$

that is related to the eddy covariance as:

$$\mathbf{C}_{ab} = \begin{pmatrix} \Delta_a \Delta_b S_{ab}^{\psi\psi} & \Delta_a \Delta_{\lambda,b} S_{ab}^{\psi\theta} \\ \Delta_{\lambda,a} \Delta_b S_{ab}^{\theta\psi} & \Delta_{\lambda,a} \Delta_{\lambda,b} S_{ab}^{\theta\theta} \end{pmatrix}, \quad (3.10)$$

we can express the Reynolds stress divergences as:

$$\begin{aligned} R^\psi(\mathbf{C}) &\stackrel{\text{def}}{=} \langle J(\psi', \zeta') + J(\theta', \Delta\theta') \rangle = \partial_x \left[\frac{1}{2} (-\partial_{y_a} \Delta_b - \partial_{y_b} \Delta_a) (S_{ab}^{\psi\psi} + S_{ab}^{\theta\theta}) \right]_{\mathbf{x}_a = \mathbf{x}_b} \\ &\quad + \partial_y \left[\frac{1}{2} (\partial_{x_a} \Delta_b + \partial_{x_b} \Delta_a) (S_{ab}^{\psi\psi} + S_{ab}^{\theta\theta}) \right]_{\mathbf{x}_a = \mathbf{x}_b}, \end{aligned} \quad (3.11)$$

$$\begin{aligned} R^\theta(\mathbf{C}) &\stackrel{\text{def}}{=} \langle J(\psi', \eta') + J(\theta', \zeta') \rangle = \\ &= \partial_x \left[\frac{1}{2} (-\partial_{y_a} \Delta_{\lambda,b} - \partial_{y_b} \Delta_a) S_{ab}^{\psi\theta} + \frac{1}{2} (-\partial_{y_a} \Delta_b - \partial_{y_b} \Delta_{\lambda,a}) S_{ab}^{\theta\psi} \right]_{\mathbf{x}_a = \mathbf{x}_b} + \\ &\quad + \partial_y \left[\frac{1}{2} (\partial_{x_a} \Delta_{\lambda,b} + \partial_{x_b} \Delta_a) S_{ab}^{\psi\theta} + \frac{1}{2} (\partial_{x_a} \Delta_b + \partial_{x_b} \Delta_{\lambda,a}) S_{ab}^{\theta\psi} \right]_{\mathbf{x}_a = \mathbf{x}_b}, \end{aligned} \quad (3.12)$$

where the subscripts a denote the action of the differential operators on \mathbf{x}_a , and $\mathbf{x}_a = \mathbf{x}_b$ denotes that the function of the two points \mathbf{x}_a and \mathbf{x}_b is to be evaluated at the same point. The first cumulant therefore evolves as:

$$(\partial_t + \mathbf{U}^\psi \cdot \nabla) Z + (\mathbf{U}^\theta \cdot \nabla) \Delta\theta + \beta V^\psi = R^\psi(\mathbf{C}) - Z, \quad (3.13)$$

$$(\partial_t + \mathbf{U}^\psi \cdot \nabla) H + (\mathbf{U}^\theta \cdot \nabla) Z + \beta V^\theta = R^\theta(\mathbf{C}) - H, \quad (3.14)$$

and in the limit of an infinite ensemble, the second cumulant \mathbf{C} evolves according to the free of fluctuations time-dependent Lyapunov equation:

$$\partial_t \mathbf{C}_{ab} = \mathbf{A}_a \mathbf{C}_{ab} + (\mathbf{A}_b \mathbf{C}_{ab}^T)^T + \mathbf{Q}_{ab}, \quad (3.15)$$

with

$$\mathbf{Q}_{ab} = \begin{pmatrix} \langle \xi_a^\psi \xi_b^\psi \rangle & 0 \\ 0 & \langle \xi_a^\theta \xi_b^\theta \rangle \end{pmatrix} = \begin{pmatrix} (1+p)\Xi(\mathbf{x}_a - \mathbf{x}_b) & 0 \\ 0 & (1-p)\Xi(\mathbf{x}_a - \mathbf{x}_b) \end{pmatrix}, \quad (3.16)$$

the homogeneous spatial covariance of the stochastic forcing. The subscript a in \mathbf{A} denotes that the differential operators in \mathbf{A} act on the variables \mathbf{x}_a of \mathbf{C}_{ab} and also that the functions in \mathbf{A} are evaluated at \mathbf{x}_a . Equations (3.13)-(3.15) form the S3T dynamical system which governs the joint evolution of the large-scale flow field described by $[Z, H]^T$ and the covariance \mathbf{C} of the eddy field and is a second order closure of the SSD, as the quasi-linear approximation to the dynamics amounts to ignoring the third and higher order cumulants in the SSD.

4. S3T stability of the homogeneous equilibrium

The statistical stationary states of the turbulent flow are manifestations of the fixed points of the SSD. If the fixed points of the SSD are stable then the turbulent flow is expected to remain close to this stationary state. If the fixed points are unstable, then the instability manifests as a transition in the turbulent flow and the new fixed points that result from the equilibration of the SSD instability correspond to the new attractor in the turbulent flow. Therefore the regime transitions from the homogeneous turbulent flow that are observed as the energy input rate increases should correspond to the instability of a

homogeneous fixed point of the SSD and the dominant structures should be manifestations of the new fixed points of the SSD.

Under homogeneous excitation, the state with no mean flow $Z = H = 0$ and homogeneous covariance $\mathbf{C}_E = \mathbf{Q}/2$, with \mathbf{Q} the excitation covariance (3.16), is a fixed point of the S3T system (3.13)-(3.15). This is the homogeneous statistical equilibrium of the two-layer fluid. We study the stability of this equilibrium as the energy input rate of the excitation, ε , is increased. The linear stability is addressed by performing an eigenanalysis of the S3T system linearized about this equilibrium. The eigenfunctions have both a mean flow component and a perturbation covariance component. The homogeneity of the equilibrium implies that the mean flow component of the eigenfunctions consists of sinusoidal functions:

$$[\delta\Psi, \delta\Theta]^T = [a_\psi, a_\theta]^T e^{i\mathbf{n}\cdot\mathbf{x}} e^{\sigma t}, \quad (4.1)$$

and the covariance eigenfunction component also consists of sinusoidal functions of the form:

$$[\delta S^{\psi\psi}, \delta S^{\psi\theta}, \delta S^{\theta\psi}, \delta S^{\theta\theta}]^T = \frac{e^{i\mathbf{n}\cdot\frac{\mathbf{x}_a+\mathbf{x}_b}{2}+\sigma t}}{2\pi} \int_{-\infty}^{\infty} \int_{-\infty}^{\infty} [\hat{S}^{\psi\psi}, \hat{S}^{\psi\theta}, \hat{S}^{\theta\psi}, \hat{S}^{\theta\theta}]^T e^{i\mathbf{k}\cdot(\mathbf{x}_a-\mathbf{x}_b)} d^2\mathbf{k}, \quad (4.2)$$

with $\mathbf{n} = (n_x, n_y)$ the wavevector of the eigenfunction, and $n = |\mathbf{n}|$ the total wavenumber. The inhomogeneity of the covariance eigenfunction is revealed by its dependence on the mean position $(\mathbf{x}_a + \mathbf{x}_b)/2$. The eigenvalue σ associated with \mathbf{n} governs the stability of perturbation (4.1), (4.2) to the homogeneous equilibrium state; the growth rate of this perturbation is $\sigma_r \stackrel{\text{def}}{=} \text{Re}(\sigma)$ and its frequency is $\sigma_i \stackrel{\text{def}}{=} \text{Im}(\sigma)$.

It is shown in Appendix A that the eigenfunctions are either purely barotropic ($a_\psi \neq 0$, $a_\theta = 0$) or purely baroclinic ($a_\psi = 0$, $a_\theta \neq 0$). The barotropic modes satisfy the dispersion relation:

$$\sigma + 1 - i\beta n_x/n^2 = f_\psi(\sigma), \quad (4.3)$$

while the baroclinic modes satisfy:

$$\sigma + 1 - i\beta n_x/n_\lambda^2 = f_\theta(\sigma), \quad (4.4)$$

with $n_\lambda \stackrel{\text{def}}{=} \sqrt{n^2 + 2\lambda^2}$. The terms f_ψ , f_θ represent the eddy acceleration feedback on the barotropic and baroclinic mean flow induced upon perturbing the equilibrium by the mean flow eigenfunction. These feedbacks are shown in Appendix A to be:

$$\begin{aligned} f_\psi(\sigma) = & \frac{1+p}{4\pi n^2} \int_{-\infty}^{\infty} \int_{-\infty}^{\infty} \frac{(n_y k_x - n_x k_y)^2 (k_{++}^2 - k^2)(1 - n^2/k^2) \hat{\Xi}}{(\sigma + 2)k^2 k_{++}^2 + i\beta(k_x k_{++}^2 - k_{x++} k^2)} d^2\mathbf{k} \\ & + \frac{1-p}{4\pi n^2} \int_{-\infty}^{\infty} \int_{-\infty}^{\infty} \frac{(n_y k_x - n_x k_y)^2 (k_{++}^2 - k^2)(1 - n^2/k_\lambda^2) \hat{\Xi}}{(\sigma + 2)k_\lambda^2 k_{++}^2 + i\beta(k_x k_{++}^2 - k_{x++} k_\lambda^2)} d^2\mathbf{k}, \end{aligned} \quad (4.5)$$

and

$$\begin{aligned} f_\theta(\sigma) = & \frac{1+p}{4\pi n_\lambda^2} \int_{-\infty}^{\infty} \int_{-\infty}^{\infty} \frac{(n_y k_x - n_x k_y)^2 (k_{++}^2 - k^2)(1 - n_\lambda^2/k^2) \hat{\Xi}}{(\sigma + 2)k^2 k_{++}^2 + i\beta(k_x k_{++}^2 - k_{x++} k^2)} d^2\mathbf{k} \\ & + \frac{1-p}{4\pi n_\lambda^2} \int_{-\infty}^{\infty} \int_{-\infty}^{\infty} \frac{(n_y k_x - n_x k_y)^2 (k_{++}^2/k_\lambda^2 - 1)(k^2 - n^2) \hat{\Xi}}{(\sigma + 2)k_\lambda^2 k_{++}^2 + i\beta(k_x k_{++}^2 - k_{x++} k_\lambda^2)} d^2\mathbf{k}, \end{aligned} \quad (4.6)$$

with the notation: $k_\lambda^2 = 1 + 2\lambda^2$, $k_{x++} = k_x + n_x$, $k_{++}^2 = |\mathbf{k} + \mathbf{n}|^2$ and $k_{\lambda++}^2 = |\mathbf{k} + \mathbf{n}|^2 + 2\lambda^2$.

Both f_ψ and f_θ are linear functions of the energy input rate ε and the S3T homogeneous equilibrium becomes unstable when these feedbacks have positive real part and the

energy input rate, ε , exceeds a critical value ε_c . The critical value, ε_c , is obtained by first determining the energy input rate $\varepsilon_t(\mathbf{n})$ for which the eigenfunction \mathbf{n} is neutral (satisfying $\sigma_r(\mathbf{n}) = 0$), and then determining the barotropic or baroclinic eigenfunction \mathbf{n} that achieves neutrality with the least energy and set $\varepsilon_c = \min(\varepsilon_t(\mathbf{n}))$.

For a single layer barotropic fluid, the dispersion properties were found to depend on the value of the non-dimensional planetary vorticity gradient β . For $\beta \ll 1$ or $\beta = \mathcal{O}(1)$ stationary zonal jets grow at the fastest rate, while for large values of β non-zonal westward propagating structures are more unstable. The same behaviour is observed for the two-layer fluid as well.

We first consider $\beta = 100$ and an uncorrelated forcing between the two layers ($p = 0$). For $\lambda \geq 0.68$ only barotropic modes become unstable when the energy input rate passes a critical value, while baroclinic modes are stable for all values of ε . Therefore the absence of baroclinic structures when $\tilde{\lambda} = \tilde{k}_f$ ($\lambda = 1$) in the NL simulations is due to the stability of the homogeneous equilibrium to baroclinic perturbations. The growth rate and frequency of the unstable barotropic modes as a function of the mean flow wavenumber \mathbf{n} are shown in figure 9 for two values of ε ($\varepsilon = 10\varepsilon_c$ and $\varepsilon = 50\varepsilon_c$) and for $\lambda = 1$. At low supercriticality (cf. figure 9a) only non-zonal modes ($n_x \neq 0$) are unstable with two branches of instability: one at meridional scales comparable to the forcing scale ($n_y \simeq 1$) and one at larger meridional scales, with the most unstable modes having larger scales than that of the excitation. The frequencies of the unstable modes are very close to the frequencies of the free barotropic Rossby waves $\sigma_{Rt} = \beta n_x / n^2$. This can be quantified by calculating the ratio $R_{ft} = \sigma_i / \sigma_{Rt}$, which is plotted in figure 9b. At larger supercriticality (cf. figure 9b) the two branches merge, stationary ($\sigma_i = 0$) barotropic zonal jet eigenfunctions ($n_x = 0$) become unstable and there is an additional branch of unstable non-zonal modes with zonal wavenumbers comparable to the excitation wavenumber ($n_x \simeq 1$) with the frequency of these modes departing substantially from the Rossby wave frequency (cf. figure 9d). However, the large-scale non-zonal structures, remain the most unstable modes.

When $\lambda < 0.68$, baroclinic modes become S3T unstable and have for small values of λ comparable growth rate to the barotropic modes (or nearly equal in the case $\lambda \ll 1$). The growth rate and frequency of the most unstable barotropic and baroclinic modes are shown in figures 10-11 for $\lambda = 0.1$, that is when the Rossby radius of deformation is ten times larger than the scale of excitation. The barotropic and baroclinic modes have similar growth rates as a function of \mathbf{n} . Their dispersion properties resemble the large-scale branch of the unstable barotropic modes at larger values of λ , with the frequencies of the large-scale modes following the dispersion of the barotropic σ_{Rt} , and baroclinic $\sigma_{Rc} = \beta n_x / n_\lambda^2$ Rossby waves as shown in figure 10c,d. At larger supercriticalities, stationary barotropic and baroclinic zonal jet eigenfunctions are unstable but the non-zonal modes have larger growth rates (cf. figure 11).

We now consider $\beta = 1$. Baroclinic modes are unstable for $\lambda < 0.37$ instead of $\lambda < 0.68$ at $\beta = 100$ and the baroclinic unstable modes have lower growth rates than the barotropic modes. This is illustrated in figure 12 where the growth rate and frequency of the unstable barotropic and baroclinic modes are shown for $\lambda = 0.1$. As in a one layer fluid, the most unstable modes are stationary zonal jets for $\beta = \mathcal{O}(1)$. For $\lambda > 0.37$ the dispersion properties of the barotropic unstable modes are similar and are not shown.

We finally test the sensitivity of the dispersion properties of the unstable modes to the forcing correlation between the two layers. Consider first the barotropic forcing ($p = 1$). In this case the flux feedbacks arise only from the first terms in (4.5)-(4.6), that is only from the organization of the barotropic turbulent eddies by the mean flow. For $\lambda = \mathcal{O}(1)$ the baroclinic modes are stable and the dispersion properties of the barotropic modes are similar to the ones shown in figure 9 with the only significant difference being the absence

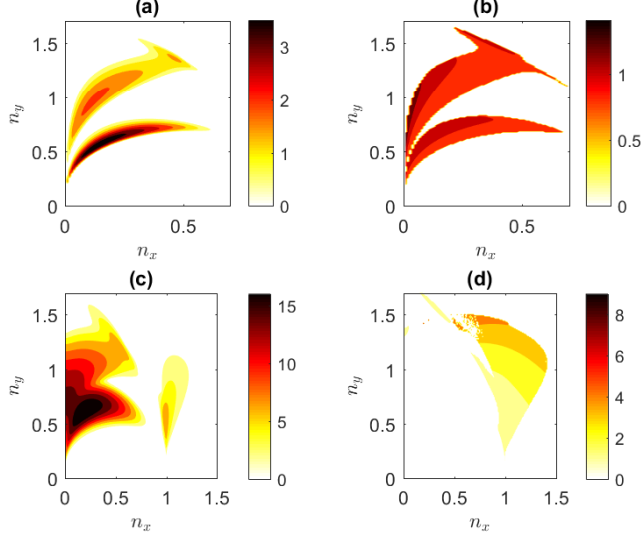


FIGURE 9. Dispersion properties of the unstable barotropic modes for $\beta = 100$, $\lambda = 1$. (a) and (c) Growth rate σ_r of the most unstable modes for (a) $\varepsilon = 10\varepsilon_c$ and (c) $\varepsilon = 100\varepsilon_c$. (b) and (d) Ratio of the frequency of the most unstable modes over the corresponding barotropic Rossby wave frequency $R_{ft} = \sigma_i/\sigma_{Rt}$ for (b) $\varepsilon = 10\varepsilon_c$ and (d) $\varepsilon = 100\varepsilon_c$. The forcing in the two layers is uncorrelated ($p = 0$).

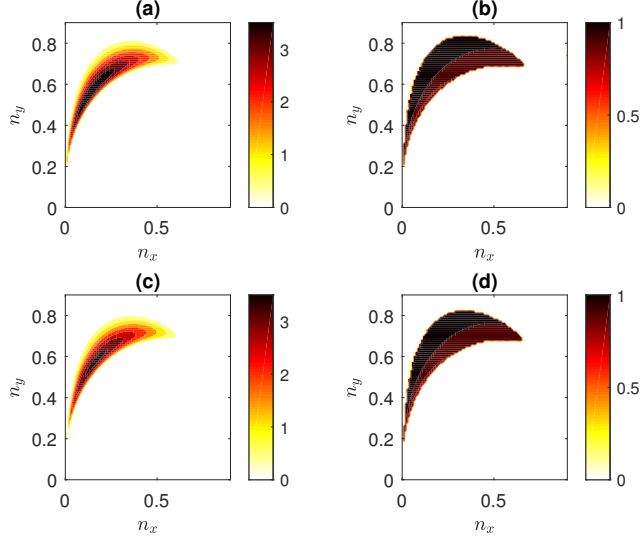
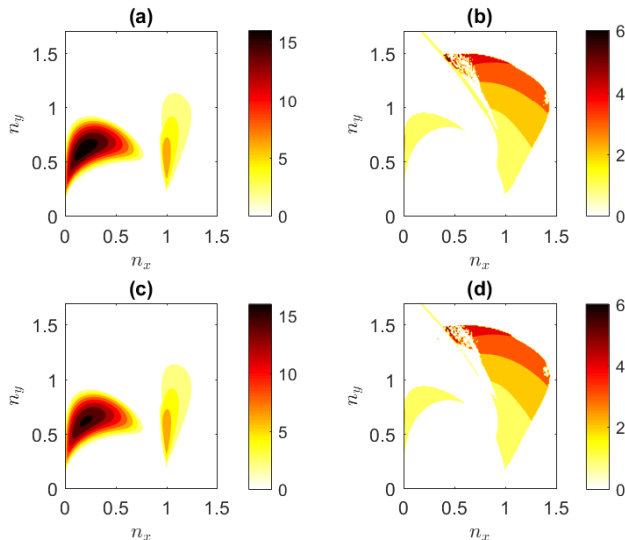


FIGURE 10. Dispersion properties of the unstable modes for $\beta = 100$, $\lambda = 0.1$ and $\varepsilon = 10\varepsilon_c$. (a) and (c) Growth rate σ_r of the most unstable (a) barotropic and (c) baroclinic modes. (b) and (d) Ratio of the frequency of the most unstable (b) barotropic modes over the corresponding barotropic Rossby wave frequency $R_{ft} = \sigma_i/\sigma_{Rt}$ and (d) baroclinic modes over the corresponding baroclinic Rossby wave frequency $R_{fc} = \sigma_i/\sigma_{Rc}$. The forcing in the two layers is uncorrelated ($p = 0$).

FIGURE 11. The same as figure 10 but for $\varepsilon = 100\varepsilon_c$.

of the upper branch. For lower values of λ , the baroclinic modes become unstable and have dispersion properties similar to the ones shown in figure 10-11 for uncorelated forcing despite the fact that small scale incoherent baroclinic eddies are not directly excited in this case ($S_E^{\theta\theta} = 0$). Therefore the instability of the baroclinic modes when excitation occurs at much smaller scales than the Rossby radius of deformation is robust regardless of whether incoherent baroclinic eddies are supported at the homogeneous equilibrium.

We then consider the baroclinic forcing ($p = -1$), in which case the flux feedbacks arise only from the organization of the baroclinic turbulent eddies by the mean flow (i.e the second terms in (4.5)-(4.6)). For low values of λ , the dispersion properties of both the barotropic and the baroclinic modes are similar to the ones obtained for uncorrelated forcing ($p = 0$) (shown in figure 10) and are not shown. The dispersion properties at $\lambda = 1$ are shown in figure 13(a)-(b). We observe that barotropic modes have faster growth rates and resemble the upper branch of figure 9, that is they have small zonal scales and meridional scales comparable to the forcing scale ($n_y \simeq 1$). The most unstable baroclinic modes, that are suboptimal compared to their barotropic counterparts, have both zonal and meridional scales comparable to the forcing scale. Interestingly, when we force at scales larger than the Rossby radius of deformation ($\lambda > 1$), the instability characteristics change. As illustrated in figure 13(c)-(d) showing the dispersion properties at $\lambda = 2$, the most unstable modes are barotropic zonal jets with scales comparable to the deformation scale, a characteristic that is also evident at even larger values of λ (not shown).

In summary, S3T predicts that the homogeneous statistical equilibrium of a two-layer baroclinic flow becomes unstable at a critical value of the energy input rate, ε_c , whereupon large-scale mean flows emerge. Barotropic modes have larger growth rates compared to their baroclinic counterparts for all values of β and λ regardless of the characteristics of the eddies supported at statistical equilibrium. When energy is injected at a length scale close to the deformation radius, barotropic modes following the Rossby wave dispersion have in general the largest growth rate for large values of β and stationary zonal jets have the largest growth rate for $\beta = \mathcal{O}(1)$. When energy is injected at scales much smaller

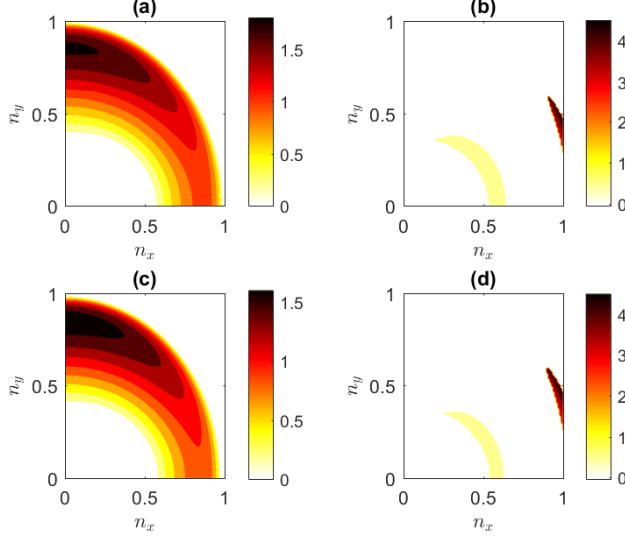


FIGURE 12. Dispersion properties of the unstable modes for $\beta = 1$, $\lambda = 0.1$ and $\varepsilon = 10\varepsilon_c$. (a) and (c) Growth rate σ_r of the most unstable (a) barotropic and (c) baroclinic modes. (b) and (d) Frequency σ_i of the most unstable (b) barotropic modes and (d) baroclinic modes. The forcing in the two layers is uncorrelated ($p = 0$).

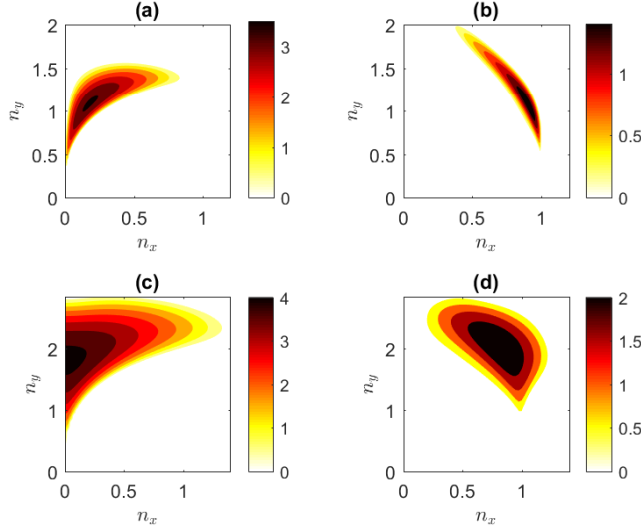


FIGURE 13. Dispersion properties of the unstable modes for baroclinic forcing ($p = -1$) at $\beta = 100$ and $\varepsilon = 10\varepsilon_c$. (a) and (b) Growth rate σ_r of the most unstable (a) barotropic and (b) baroclinic modes for $\lambda = 1$. (c) and (d) Growth rate σ_r of the most unstable (c) barotropic and (d) baroclinic modes when $\lambda = 2$.

than the deformation radius, both barotropic and baroclinic large-scale flows emerge with the barotropic modes having slightly larger growth rates.

5. Equilibration of the SSD instabilities and comparison to NL simulations

In this section we examine the equilibration of the SSD instabilities by numerical integrations of the S3T dynamical system. The goal is twofold. The first is to determine the non-homogeneous fixed points of the S3T dynamical system with the largest domain of attraction that a random perturbation will likely end up to. For example, we saw in the previous section that when the non-dimensional radius of deformation is smaller than a critical value, barotropic and baroclinic modes have comparable growth rates. Therefore there is the question of whether the equilibrated state will consist of both barotropic and baroclinic components. The second is to compare the dominant structures in the turbulent flow with the equilibrated states in the S3T system and to investigate whether the characteristics of the dominant structures in the NL simulations are predicted by S3T.

To integrate the S3T dynamical system, we discretize (3.13)-(3.15) in a doubly periodic channel of size $2\pi \times 2\pi$ using a pseudo-spectral code and a fourth order time-stepping Runge-Kutta scheme. Due to the high-dimensionality of the covariance matrix we use the modest $M = 32 \times 32$ resolution. To facilitate the comparison with the NL simulations, we apply the same ring forcing (3.1) and consider the same parameters $\tilde{\beta} = 60$, $\tilde{r} = 0.1$, $\tilde{k}_f = 6$ and $\Delta\tilde{k}_f = 1$. Because the S3T simulations are computationally expensive, we also utilize for comparison purposes simulations of the ensemble quasi-linear system (EQL) defined in (3.2), (3.3), (3.6). The EQL system is the finite ensemble version of the deterministic S3T dynamical system and the EQL simulations converge to the S3T integrations as the number of ensemble members N_{ens} used to calculate the mean increases. The emergent structures and the statistical turbulent equilibria predicted by the S3T system manifest in the EQL integrations with the addition of noise from stochastic forcing fluctuations, which for any finite N_{ens} do not average to zero. A disadvantage of this method is that due to thermal noise from the excitation, only the equilibria with the largest domain of attraction will emerge. Previous studies have investigated the convergence of the EQL simulations to the S3T integrations and determined that $N_{\text{ens}} = 10$ ensemble members illustrate the relevant dynamics with minimal computational cost (Bakas & Ioannou 2014; Constantinou *et al.* 2016)). We therefore make the same choice.

Consider first the case of uncorrelated forcing between the layers ($p = 0$) and $\tilde{\lambda} = \tilde{k}_f$. The critical energy input rate $\tilde{\varepsilon}_c$ that renders the homogeneous S3T equilibrium unstable is obtained from the discrete version of equations (4.3)-(4.4). We investigate the equilibration of the SSD instability for supercritical values of $\tilde{\varepsilon}$ through S3T integrations. For $\tilde{\varepsilon} = 2\tilde{\varepsilon}_c$, the barotropic perturbation with $(\tilde{n}_x, \tilde{n}_y) = (1, 4)$ has the largest growth rate, while the baroclinic perturbations are S3T stable at this value of $\tilde{\lambda}$ for all values of $\tilde{\varepsilon}$. At $t = 0$, we introduce a small random perturbation, with both barotropic and baroclinic mean flow components and study the evolution of the energy of the baroclinic and barotropic components through the baroclinicity measure:

$$R_b = \frac{\sum_{\tilde{k}_x, \tilde{k}_y} (\tilde{k}^2 + 2\tilde{\lambda}^2) |\hat{\Theta}(\tilde{\mathbf{k}})|^2}{\sum_{\tilde{k}_x, \tilde{k}_y} \tilde{k}^2 |\hat{\Psi}(\tilde{\mathbf{k}})|^2}, \quad (5.1)$$

in which $\hat{\Psi}$ and $\hat{\Theta}$ are the Fourier components of the barotropic and baroclinic mean flow streamfunction respectively. As shown in figure 14a, the baroclinicity, R_b , decays exponentially and the baroclinic part of the flow diminishes as predicted by the S3T stability analysis, while the energy of the barotropic flow, also shown in figure 14a, grows exponentially with the predicted growth rate, and the flow finally equilibrates to a westward propagating wave. The barotropic streamfunction at equilibrium, shown

in figure 14b, has Fourier components primarily with wavenumbers $(|\tilde{k}_x|, |\tilde{k}_y|) = (1, 4)$ and secondarily with wavenumbers $(|\tilde{k}_x|, |\tilde{k}_y|) = (2, 4)$. Investigation of the propagation properties of the wave shows that the phase speed of each wave component is very close to the phase speed of the unstable modes that themselves are nearly equal to the Rossby wave phase speed for each component.

The finite amplitude state of the SSD consisting of the propagating waves becomes itself secondarily unstable at larger energy input rates to zonal jet perturbations. This secondary SSD instability has already been discussed in the context of a single layer barotropic flow on a β -plane by Bakas & Ioannou (2014) and for the chosen parameters it occurs at $\tilde{\varepsilon}_{nl} = 15\tilde{\varepsilon}_c$. The flow then transitions to a new equilibrium state such as the one shown in figure 14c,d for the case $\tilde{\varepsilon} = 60\tilde{\varepsilon}_c$. This state consists of a zonal jet (figure 14c) coexisting with a weak propagating wave (figure 14d), as in single layer barotropic flows (Bakas & Ioannou 2014; Constantinou *et al.* 2016).

We now investigate how these results relate to the regime transitions and to the characteristics of the dominant structures in the turbulent flow. The rapid increase of the nzmf index in the NL simulations when the energy input rate passes the critical value $\tilde{\varepsilon}_c$ calculated from the stability analysis of the homogeneous fixed point of the SSD shows that the bifurcation point for the emergence of large scale waves in the turbulent flow is accurately predicted by S3T. The same holds for the increase of the zmf index observed in figure 1 for $\tilde{\varepsilon} \gtrsim 12\tilde{\varepsilon}_c$, which shows that zonal jets emerge in the flow approximately at the stability threshold $\tilde{\varepsilon}_{nl}$ of the finite amplitude traveling wave states. The small quantitative discrepancy observed should be attributed to both the thermal noise in the NL simulations and in the quasi-linear approximation of the dynamics. The scales and phase speeds of the dominant large scale structures in the NL simulations also match the scales and phase speeds of the equilibrated SSD instabilities in S3T. This is illustrated by comparing the distinct peaks in the kinetic energy power spectra in the NL simulations and the frequency power spectrum of the wave components shown in figures 3-4 to the scales of the emergent structures in the S3T simulations shown in figure 14 and their phase speed. In order to compare the amplitude of the emergent structures we calculate the equivalent kinetic energy power spectra

$$\hat{E}_{S3T}^{\psi}(\tilde{\mathbf{k}}) = \tilde{k}^2 \left(|\hat{\Psi}|^2 + \hat{S}^{\psi\psi} \right), \quad (5.2)$$

$$\hat{E}_{S3T}^{\theta}(\tilde{\mathbf{k}}) = \tilde{k}^2 \left(|\hat{\Theta}|^2 + \hat{S}^{\theta\theta} \right), \quad (5.3)$$

where $\hat{S}^{\psi\psi}$ and $\hat{S}^{\theta\theta}$ are the power spectra of the eddy covariances $S^{\psi\psi}$ and $S^{\theta\theta}$ respectively. For the barotropic part, the eddy power spectrum $\hat{S}^{\psi\psi}$ shown in figure 15a and d is two orders of magnitude smaller than $|\hat{\Psi}|^2$, so the equivalent power spectrum \hat{E}_{S3T}^{ψ} shown in figure 15b and e is dominated by the spectrum of the coherent part of the flow. This should come as no surprise, since the dominant structures in the turbulent flow are phase coherent and should therefore be a manifestation of the coherent part of the flow Ψ . For the baroclinic part, $\Theta = 0$, so \hat{E}_{S3T}^{θ} that is shown in figure 15c and e coincides with the eddy power spectrum $\hat{S}^{\theta\theta}$. Comparison of the spectra obtained from the NL simulations (figures 3 and 4) and the equivalent spectrum shown in figure 15 shows that the amplitude of the emergent structures differs by a factor of two for $\tilde{\varepsilon} = 2\tilde{\varepsilon}_c$ and by about 20% for $\tilde{\varepsilon} = 60\tilde{\varepsilon}_c$. To facilitate comparison of the amplitude of the emerging structures for a wide range of values for the energy input rate, we utilize the EQL simulations and calculate the zmf and nzmf indices that are shown in figure 1. We observe that apart from the quantitative disagreement at low supercritical energy input rates for the amplitude of the emergent waves, the EQL dynamics fairly reproduce the amplitude of the emergent structures.

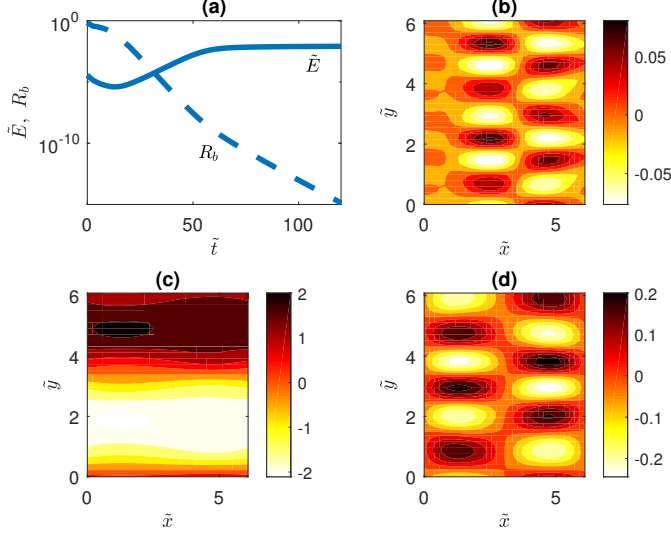


FIGURE 14. (a) Evolution of the mean flow energy \tilde{E} (solid line) and baroclinicity R_b defined in (5.1) (dashed line) and (b) contours of mean flow barotropic streamfunction $\tilde{\Psi}$ at equilibrium for $\tilde{\varepsilon} = 2\tilde{\varepsilon}_c$. (c) Contours of mean flow barotropic streamfunction $\tilde{\Psi}$ at equilibrium and (d) non-zonal part of the equilibrium streamfunction when $\tilde{\varepsilon} = 60\tilde{\varepsilon}_c$. The parameters values are the same as in figure 1.

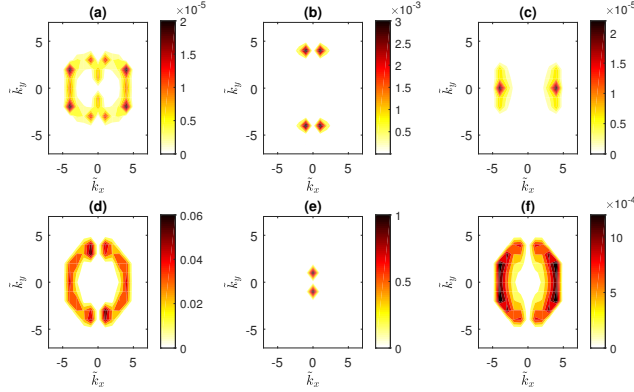


FIGURE 15. (a) Kinetic energy power spectrum of the barotropic part of the eddy covariance $k^2 \hat{S}^{\psi\psi}$, (b) total kinetic energy power spectrum \hat{E}_{S3T}^{ψ} of the barotropic part of the flow and (c) total kinetic energy power spectrum \hat{E}_{S3T}^{θ} of the baroclinic part of the flow for $\tilde{\varepsilon} = 2\tilde{\varepsilon}_c$. (d)-(f) The same as in (a)-(c) but for $\tilde{\varepsilon} = 60\tilde{\varepsilon}_c$.

Similar results regarding the comparison of the S3T prediction with NL simulations were found for barotropic turbulence in Bakas & Ioannou (2014), showing that the quasi-linear dynamics close to the bifurcation point capture the emergence of flows in contrast to the physical intuition on the importance of the non-linear terms as also discussed in the introduction.

Consider now $\tilde{\lambda} = \tilde{k}_f/6$ ($\lambda = 1/6$) for which the S3T stability analysis predicts the existence of both barotropic and baroclinic unstable S3T modes. We have identified in this case three attracting equilibrium states with finite amplitude mean flows. The first is a

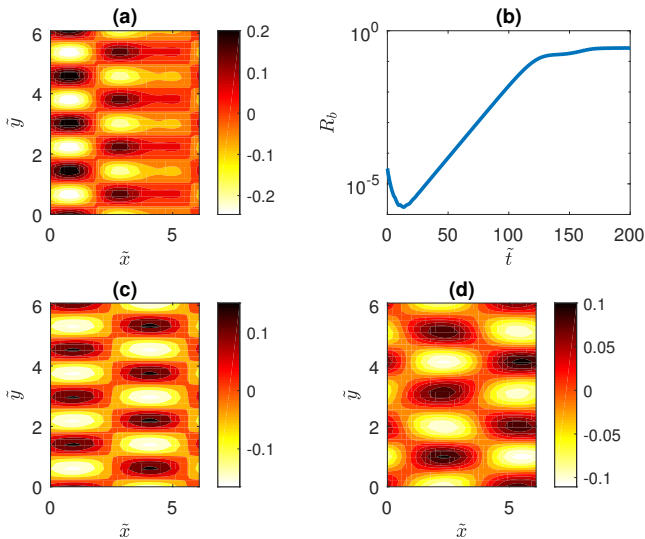


FIGURE 16. (a) Contours of mean flow barotropic streamfunction Ψ for the pure barotropic equilibrated state. (b) Evolution of the baroclinicity ratio after inserting a baroclinic mean flow perturbation to the barotropic equilibrium shown in (a). (c)-(d) Contours of mean flow (c) barotropic Ψ and (d) baroclinic Θ streamfunction for the mixed barotropic-baroclinic equilibrium state. The energy input rate is $\tilde{\varepsilon} = 10\tilde{\varepsilon}_c$, $\tilde{\lambda} = \tilde{k}_f/6$ and the rest of the parameters are as in figure 14.

purely barotropic equilibrium, to which all purely barotropic perturbations are attracted. Note that purely barotropic perturbations do not produce any baroclinic fluxes even in their nonlinear stage of evolution and as a result, the mean flow remains barotropic. An example of such an equilibrated state is shown for $\tilde{\varepsilon} = 10\tilde{\varepsilon}_c$ in figure 16a, where again the large-scale flow is a westward propagating wave. However this equilibrium is secondarily unstable to baroclinic mean flow perturbations. We illustrate this by perturbing the barotropic equilibrium, shown in figure 16a, with a small baroclinic mean flow perturbation. Figure 16b shows that the baroclinic mean flow component grows exponentially at first and as soon as it reaches a finite amplitude, the flow transitions to the second non-zonal equilibrium with both barotropic and baroclinic components and baroclinicity $R_b \simeq 1/4$. The structure of these components is shown in figure 16c,d.

The third equilibrium is also a westward propagating wave with both barotropic and baroclinic components and similar scale as the one shown in figure 16c,d but is more baroclinic ($R_b \simeq 2$). However, this equilibrium has a very small domain of attraction and it can be approached only if the initial perturbation is baroclinic[†]. As a result, we do not expect this equilibrium to manifest in noisy simulations of the turbulent flow in which both baroclinic and barotropic perturbations inevitably arise. Therefore, at low supercriticalities the S3T instabilities equilibrate to the finite amplitude mixed barotropic-baroclinic traveling wave shown in figure 16c,d with baroclinic to barotropic streamfunction amplitude ratio of about one half.

Again, at higher supercriticality the traveling baroclinic wave states of the SSD become secondarily unstable to zonal perturbations. However, only the barotropic part of the flow

[†] Specifically, this equilibrium is approached only if the initial perturbation has a baroclinicity ratio larger than 10^6 .

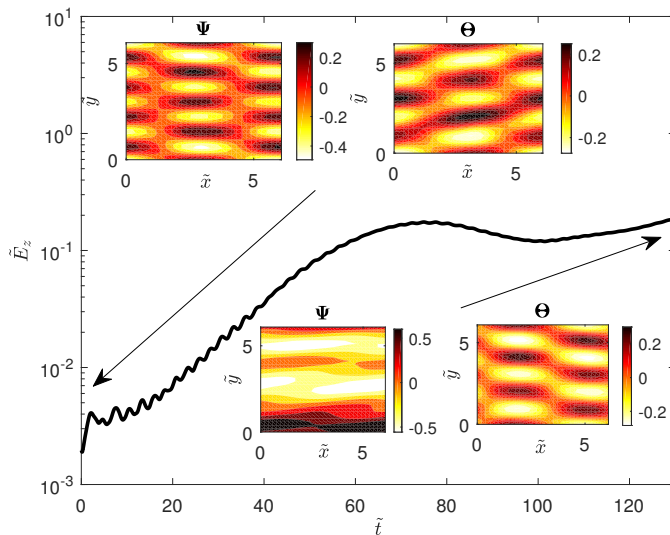


FIGURE 17. Evolution of the energy of the zonal part of the flow when a zonal mean flow perturbation is imposed on the finite amplitude equilibrium state shown in the upper insets. The lower insets show the barotropic and baroclinic streamfunction of the mean flow at $\tilde{t} = 130$. The energy input rate is $\tilde{\varepsilon} = 40\tilde{\varepsilon}_c$, and the rest of the parameters are as in figure 16.

turns into zonal jets. This is shown in the numerical integration for $\tilde{\varepsilon} = 40\tilde{\varepsilon}_c$ illustrated in figure 17. In this experiment the mixed barotropic-baroclinic traveling wave state, shown in the upper inset of figure 17, is perturbed by a zonal mean flow perturbation with both barotropic and baroclinic components. The energy of the zonal part of the flow, \tilde{E}_z , grows exponentially and the flow transitions to the state shown at the lower inset, that consists of a zonal barotropic flow and a traveling baroclinic wave. This is a time dependent state as shown in figure 18. The energy of the zonal part of the flow and the baroclinicity R_b oscillate and are anti-correlated revealing that the large scale flow vacillates between the state shown in figure 19a,b where the barotropic zonal jet is dominant and the state shown in figure 19c,d where the baroclinic wave is dominant. At even higher energy input rates the large scale flow exhibits the same time dependence but with weaker fluctuations due to the weakening of the baroclinic wave component.

Comparison of the dominant structures in the NL simulations (c.f figures 5-6) to the equilibrated states in S3T with the largest domain of attraction (c.f figures 16-19) demonstrates that the scales of the phase coherent large scale waves in the turbulent flow are predicted by S3T. Figure 20 shows the equivalent spectra which are dominated in this case as well by the coherent part of the flow. Comparison to the spectra obtained from the NL simulations (cf. figure 5) shows quantitative differences of the order of 20% for the amplitude of the emergent structures. Differences on the exact points of transition from the wave attractor to the jet attractor are found in this case as well. But even nuances of the dynamics such as the long time variability of the turbulent flow at $\tilde{\varepsilon} = 40\tilde{\varepsilon}_c$ with a vacillation between a state with stronger barotropic jet/weaker baroclinic wave and a state with a stronger baroclinic wave/weaker barotropic jet are captured in S3T with approximately the same time scale as revealed by comparison of figures 6 and 18.

We now consider the equilibration of the S3T instabilities for the other two cases of forcing correlation, that is exciting only the barotropic ($p = 1$) and the baroclinic ($p = -1$) eddies. For the case of barotropic forcing, the instability characteristics as well as their

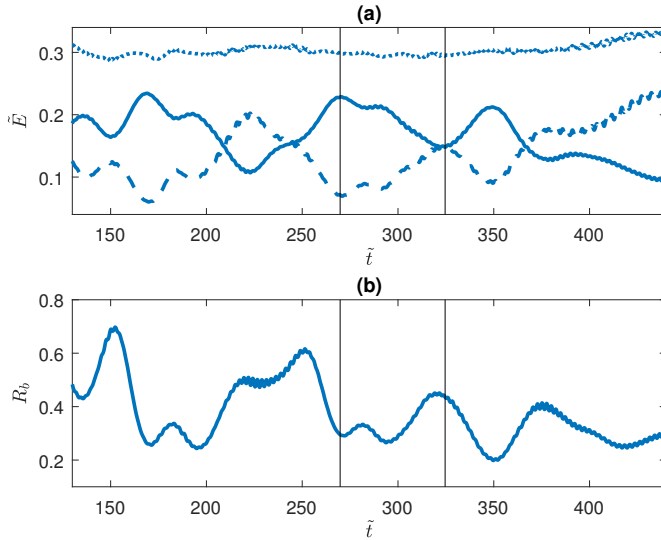


FIGURE 18. (a) Evolution of the mean flow energy (dotted), the energy of the zonal part (solid) and the energy of the non-zonal part (dashed) of the flow. (b) Evolution of the baroclinicity R_b . The vertical lines denote the times at which the snapshots shown in figure 19 are taken.

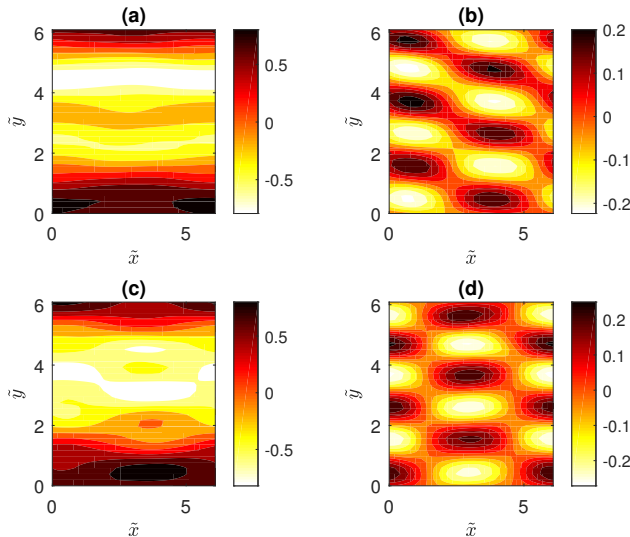


FIGURE 19. (a)-(b) Snapshot of the mean flow (a) barotropic Ψ and (b) baroclinic Θ streamfunction at $\tilde{t} = 270$. (c)-(d) The same as in (a)-(b) but for a snapshot at $\tilde{t} = 325$.

equilibration are similar to the case of uncorrelated forcing between the two layers and are not shown. For the case of baroclinic forcing, structures with small meridional scales are predicted to initially emerge and the low resolution of the S3T calculations is not adequate to resolve these scales. For this reason we choose to study the equilibration of the instabilities with ensemble quasi-linear simulations (EQL) governed by (3.2)-(3.3) and (3.6) at higher resolution (64×64).

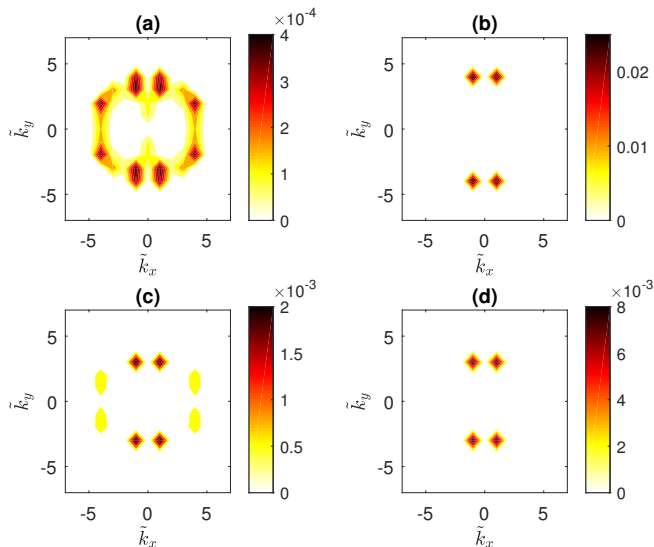


FIGURE 20. (a) Kinetic energy power spectrum of the barotropic part of the eddy covariance $k^2 \hat{S}^{\psi\psi}$. (b) Equivalent kinetic energy power spectrum \hat{E}_{S3T}^{ψ} of the barotropic part of the flow. (c) Kinetic energy power spectrum of the baroclinic part of the eddy covariance $k^2 \hat{S}^{\theta\theta}$ and (d) equivalent kinetic energy power spectrum \hat{E}_{S3T}^{θ} of the baroclinic part of the flow for $\tilde{\varepsilon} = 10\tilde{\varepsilon}_c$.

Consider first $\tilde{\lambda} = \tilde{k}_f$ ($\lambda = 1$). At low supercriticality ($\tilde{\varepsilon} < 5\tilde{\varepsilon}_c$), the baroclinic modes are stable and barotropic Rossby waves that have the largest growth rate equilibrate at finite amplitude as in the case of uncorrelated forcing. The only difference in this case is that these waves have meridional scales comparable to the forcing scale (the most unstable mode has $(|\tilde{n}_x|, |\tilde{n}_y|) = (1, 6)$). As a result the flow equilibrates to this barotropic traveling wave state. This is shown in figure 21(a)-(b) in which a snapshot of the barotropic and the baroclinic streamfunction are shown. For higher supercriticality ($\tilde{\varepsilon} > 5\tilde{\varepsilon}_c$), baroclinic modes are rendered unstable as well. However, the finite amplitude equilibria have very weak baroclinicity. This is illustrated in figure 21(c)-(d), showing that the baroclinic streamfunction is one order of magnitude smaller than the barotropic part of the flow that has been zoned through the secondary SSD instability. Consider now the larger value $\tilde{\lambda} = 2\tilde{k}_f$ ($\lambda = 2$) for which linear stability analysis predicts that barotropic stationary zonal jets with scales close to the Rossby radius of deformation have the largest growth rate. The equilibrated structure for $\tilde{\varepsilon} = 10\tilde{\varepsilon}_c$ is shown in figure 22(a)-(b). Indeed it consists of a small scale barotropic jet with a scale comparable to the deformation radius ($\tilde{n}_y = 3\tilde{\lambda}/4$) and a very weak baroclinic flow. At larger supercriticality, the jets assume larger scales (c.f. 22(c)-(d)) and baroclinicity remains weak. Finally we note that at $\tilde{\lambda} = \tilde{k}_f/6$ the equilibrated structures are similar to the case of uncorrelated forcing and are not shown.

Comparison of the coherent structures in figures 21-22 to the emergent structures in the NL simulations in figures 7-8 reveals that again the scales of the emergent flows are accurately captured by S3T, while their amplitude is slightly underestimated.

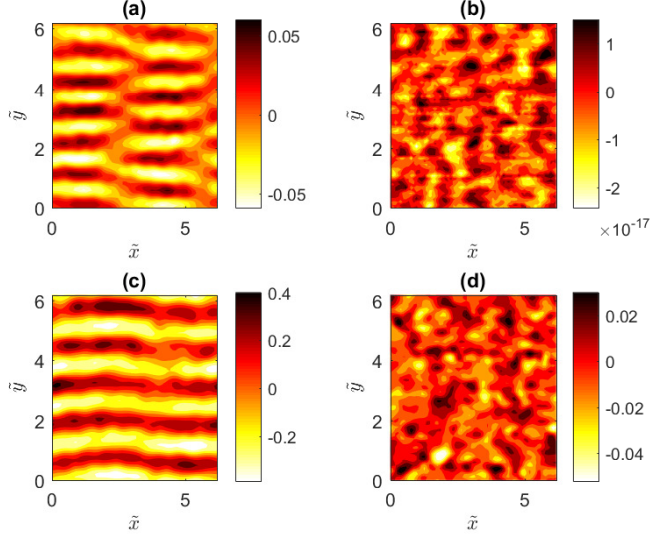


FIGURE 21. (a)-(b) Contours of the (a) barotropic Ψ and (b) baroclinic Θ streamfunction of the equilibrated state for a baroclinic forcing ($p = -1$) at $\tilde{\varepsilon} = 4\tilde{\varepsilon}_c$ and $\tilde{\lambda} = \tilde{k}_f$. (c)-(d) The same as in (a) and (b) but for $\tilde{\varepsilon} = 60\tilde{\varepsilon}_c$. The flows are obtained from EQL integrations at a 64×64 resolution and $N_{ens} = 10$ ensemble members.

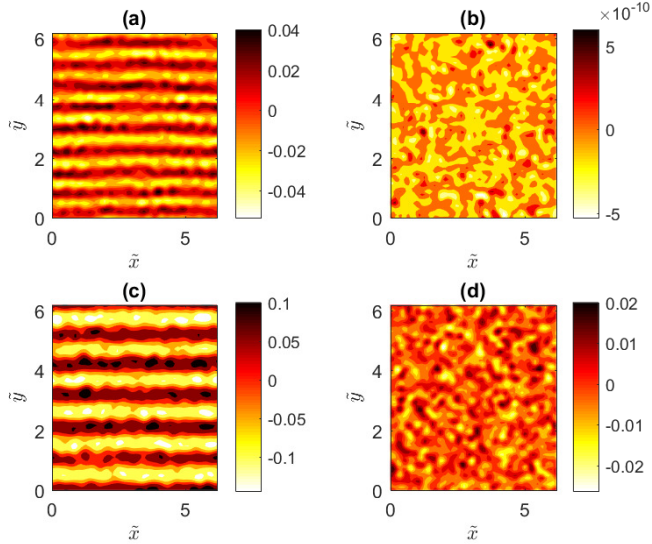


FIGURE 22. (a)-(b) Contours of the (a) barotropic Ψ and (b) baroclinic Θ streamfunction of the equilibrated state for a baroclinic forcing ($p = -1$) at $\tilde{\varepsilon} = 10\tilde{\varepsilon}_c$ and $\tilde{\lambda} = 2\tilde{k}_f$. (c)-(d) The same as in (a) and (b) but for $\tilde{\varepsilon} = 60\tilde{\varepsilon}_c$. The flows are obtained from EQL integrations at a 64×64 resolution and $N_{ens} = 10$ ensemble members.

6. Conclusions

The emergence of coherent structures in stratified turbulent flows with turbulence supported by external sources was investigated in this work. A two-layer model on a β -

plane channel was considered under the influence of homogeneous and isotropic stochastic forcing and linear damping of potential vorticity. No mean thermal gradient was imposed in the flow. The goal was to extend the analysis of previous studies which found that coherent flows emerge out of a background of homogeneous turbulence as a bifurcation when the turbulence intensity increases and that these turbulent bifurcations can be attributed to a new type of collective instability of the statistical state dynamics of the turbulent flow. The questions addressed were the following: in the absence of temperature gradients can externally forced turbulence in a stratified flow support turbulent equilibria in which large scale baroclinic coherent flows are sustained at finite amplitude? Or are the large scale flows that emerge necessarily barotropic?

Direct non-linear simulations show two major flow transitions as the energy input rate of the forcing increases. In the first transition large scale, Rossby waves that remain phase coherent over long time scales emerge in the flow. As the energy input rate increases, the scales of these waves as well as their energy increases as well. In the second transition, zonal jets emerge instead while the energy in the large scale waves decreases. Regarding the vertical structure of the emergent flows, the large scale waves and jets are barotropic when energy is injected at scales comparable to the Rossby radius of deformation. When the energy is injected at smaller scales, the waves that emerge have comparable barotropic and baroclinic streamfunctions. After the second transition, the barotropic part of the flow is zonated and the turbulent flow exhibits variability on long times scales with time periods of stronger barotropic jet and time periods of stronger baroclinic waves. For larger energy input rates the barotropic jet dominates. These results were found to be independent of the correlation of the excitation between the two layers as two extreme cases (forcing only baroclinic eddies and forcing only barotropic eddies) produced qualitatively similar results to the case of uncorrelated forcing between the two layers. That is, even though the forcing might inject barotropic eddies only in the flow, these eddies are organized as to yield baroclinic fluxes to support the baroclinic waves. Similarly, in the case in which we inject baroclinic eddies only in the flow, the prevalence of barotropic coherent structures remains.

We then developed a theory to explain the emergence of coherent flows and predict their characteristics. The theory is based on a second order closure of the statistical state dynamics (SSD) of the turbulent flow (S3T). The fixed points of the S3T dynamical system for the joint evolution of the coherent flow and the eddy covariance define equilibria, the manifestations of which are the states of the turbulent flow at statistical equilibrium. Instability of these fixed points and equilibration into new steady states of the SSD also manifest as regime transitions in the turbulent flow with the emergence of new attractors.

The linear stability of the homogeneous equilibrium with no coherent structures was examined analytically for a wide range of forcing scales $1/\tilde{k}_f$ relative to the deformation radius $1/\tilde{\lambda}$ and a wide range of values for the non-dimensional planetary vorticity gradient $\beta = \beta\tilde{r}/\tilde{k}_f$, where $1/\tilde{r}$ is the linear dissipation time scale. The equilibrium was found to be unstable for all λ when the energy input rate of the forcing exceeds a critical value. When turbulence is injected close to the Rossby radius of deformation or at larger scales, baroclinic flows are either stable or grow at a lower rate compared to barotropic flows. For large values of β , westward propagating barotropic waves that follow the barotropic Rossby wave dispersion grow the most, while for values of $\beta = \mathcal{O}(1)$ or lower stationary zonal jets have faster growth rates. The equilibration of the incipient instabilities was then studied for large values of β through numerical integrations of the S3T dynamical system. The flow was found to equilibrate for low supercriticality at finite amplitude traveling wave states that approximately have the same dispersion properties as the unstable modes.

For larger supercriticality, the traveling wave states become S3T unstable with respect to zonal jet perturbations. The flow then equilibrates at mixed jet-traveling wave states with lower amplitude traveling waves embedded in strong zonal jets. This dynamics is similar to barotropic turbulence organization that was investigated in earlier studies (Bakas & Ioannou 2014; Constantinou *et al.* 2016).

When turbulence is injected at scales much smaller than the deformation radius, barotropic and baroclinic modes have comparable growth rates with barotropic modes growing at slightly faster rates and having dispersion properties similar to the ones for larger values of the deformation radius. For low supercriticalities, the flow equilibrates at mixed barotropic-baroclinic traveling wave states with the barotropic streamfunction having a larger amplitude compared to the baroclinic streamfunction. For higher supercriticalities, a secondary S3T instability of the traveling wave states similar to the one discussed above zonates the barotropic part of the flow. As a result the flow transitions to a mixed barotropic-baroclinic jet-wave state where a weaker baroclinic wave is embedded in a stronger barotropic jet. This state is time dependent with the amplitudes of the barotropic jet and the baroclinic wave oscillating in time as the jet intensifies the wave for half a cycle and the wave intensifies the jet in the next part of the cycle giving the excess energy back to the jet. For highly supercritical regimes, the baroclinicity and this vacillation are much weaker. Finally, it was found that the characteristics of the emergent structures are not sensitive to the correlation of the forcing in the two layers (with small exceptions in the case of baroclinic forcing).

The predictions of the theory regarding the SSD were then compared to the results obtained in direct numerical nonlinear simulations. First of all, the absence of baroclinic structures in the turbulent flow when the energy is injected at scales comparable to the deformation radius, is attributed to the stability of the homogeneous equilibrium to baroclinic modes. The critical threshold above which non-zonal structures are unstable according to the stability analysis of the S3T system was found to be in excellent agreement with the critical value above which large scale, phase coherent waves acquire significant power in the nonlinear simulations. The scale and phase speed of the dominant structures in the nonlinear simulations were also found to correspond to the coherent structures predicted by S3T including the existence or not of a baroclinic component for the flow. However, the amplitude of the emerging waves is underestimated. In addition, the critical turbulence intensity threshold for the emergence of zonal jets, which is identified in S3T as the energy input rate at which the secondary instability of the finite amplitude traveling wave states appears, was also found to roughly match the corresponding threshold for jet formation in the nonlinear simulations, with the emerging jet scale being accurately obtained using S3T. As in the wave regime, the jet amplitude is underestimated by roughly 20 %. However, it is surprising that even nuances of the statistical state dynamics such as the time dependent mixed barotropic-baroclinic jet-wave state have a manifestation in the fully turbulent flow.

In summary, in stratified flows with no mean thermal gradient imposed, there is a large bias towards the emergence of barotropic flows even though both barotropic and baroclinic incoherent turbulent eddies can be supported at a homogeneous turbulent equilibrium. When turbulence is injected at the deformation radius (or larger) baroclinic mean flow perturbations to the homogeneous equilibrium do not emerge. When turbulence is injected at much smaller scales compared to the deformation radius, flows with baroclinic components emerge but the baroclinicity of the flow is rather small and the baroclinic component of the flow remains non-zonal even though the barotropic part is zonated when the turbulence intensity is above a critical threshold. It is also important to note that similar to the organization of barotropic turbulence, a second-order closure of the SSD is

very accurate in capturing the transitions in the turbulent flow with the emergence of coherent structures even in this regime in which the shear rate of the emerging mean flows is infinitesimally small. We can therefore conclude that the coherent structures emerge as instabilities of the SSD of the flow, an analytical treatment of which is only amenable in the second-order closure framework of the SSD.

Acknowledgements. The authors would like to thank Navid Constantinou for useful discussions. Nikos Bakas is supported by the AXA Research Fund.

Appendix A. Stability equation

It can be readily shown as in the barotropic case (Bakas & Ioannou 2014) that due to the homogeneity of the forcing covariance, the state with zero coherent flow $Z = H = 0$ and a homogeneous covariance $\mathbf{C}_E = \mathbf{Q}/2$ is a fixed point of the S3T dynamical system. The linear stability of the homogeneous equilibrium is assessed by considering the joint linear evolution of barotropic and baroclinic mean flow perturbations $[\delta\Psi, \delta\Theta]^T$ and covariance perturbations $\delta\mathbf{C}$. The linearized equations governing the evolution of the coherent mean flow perturbations are:

$$\partial_t \Delta \delta\Psi + \beta \partial_x \delta\Psi = \delta f_\psi - \Delta \delta\Psi, \quad (\text{A } 1)$$

$$\partial_t \Delta_\lambda \delta\Theta + \beta \partial_x \delta\Theta = \delta f_\theta - \Delta_\lambda \delta\Theta, \quad (\text{A } 2)$$

where $\delta f_\psi = R^\psi(\delta\mathbf{C})$ and $\delta f_\theta = R^\theta(\delta\mathbf{C})$ are the perturbation eddy stress divergences which depend linearly on the components of $\delta\mathbf{C}$. The components of $\delta\mathbf{C}$ evolve according to :

$$\begin{aligned} \partial_t \delta C^{\zeta\zeta} = & -2\delta C^{\zeta\zeta} - \beta \left[\partial_{\tilde{x}} \left(\tilde{\Delta} + \frac{1}{4}\bar{\Delta} \right) - 2\partial_{\tilde{x}} \Gamma \right] \delta S^{\psi\psi} - \left(\delta \mathbf{U}_a^\psi - \delta \mathbf{U}_b^\psi \right) \cdot \tilde{\nabla} \tilde{\Delta}^2 S_E^{\psi\psi} \\ & - \left(\Delta_a \delta \mathbf{U}_a^\psi - \Delta_b \delta \mathbf{U}_b^\psi \right) \cdot \tilde{\nabla} \tilde{\Delta} S_E^{\psi\psi}, \end{aligned} \quad (\text{A } 3)$$

$$\begin{aligned} \partial_t \delta C^{\zeta\eta} = & - \left[\left(\delta \mathbf{U}_a^\theta \cdot \tilde{\nabla} \right) \tilde{\Delta} \tilde{\Delta}_\lambda - \left(\Delta_a \delta \mathbf{U}_a^\theta \cdot \tilde{\nabla} \right) \tilde{\Delta}_\lambda \right] S_E^{\theta\theta} + \left[\left(\delta \mathbf{U}_b^\theta \cdot \tilde{\nabla} \right) \tilde{\Delta}^2 - \left(\Delta_{\lambda,b} \delta \mathbf{U}_b^\theta \cdot \tilde{\nabla} \right) \tilde{\Delta} \right] S_E^{\psi\psi} \\ & - 2\delta C^{\zeta\eta} - \beta \left[\frac{1}{2} \partial_{\tilde{x}} \left(\tilde{\Delta} + \tilde{\Delta}_\lambda + \frac{1}{2}\bar{\Delta} \right) - \partial_{\tilde{x}} \left(\tilde{\Delta} - \tilde{\Delta}_\lambda + 2\Gamma \right) \right] \delta S^{\psi\theta}, \end{aligned} \quad (\text{A } 4)$$

$$\begin{aligned} \partial_t \delta C^{\eta\zeta} = & \left[\left(\delta \mathbf{U}_b^\theta \cdot \tilde{\nabla} \right) \tilde{\Delta} \tilde{\Delta}_\lambda - \left(\Delta_b \delta \mathbf{U}_b^\theta \cdot \tilde{\nabla} \right) \tilde{\Delta}_\lambda \right] S_E^{\theta\theta} - \left[\left(\delta \mathbf{U}_a^\theta \cdot \tilde{\nabla} \right) \tilde{\Delta}^2 - \left(\Delta_{\lambda,a} \delta \mathbf{U}_a^\theta \cdot \tilde{\nabla} \right) \tilde{\Delta} \right] S_E^{\psi\psi} \\ & - \delta C^{\eta\zeta} - \beta \left[\frac{1}{2} \partial_{\tilde{x}} \left(\tilde{\Delta} + \tilde{\Delta}_\lambda + \frac{1}{2}\bar{\Delta} \right) - \partial_{\tilde{x}} \left(\tilde{\Delta}_\lambda - \tilde{\Delta} + 2\Gamma \right) \right] \delta S^{\theta\psi}, \end{aligned} \quad (\text{A } 5)$$

$$\begin{aligned} \partial_t \delta C^{\eta\eta} = & - \left[\left(\delta \mathbf{U}_a^\psi - \delta \mathbf{U}_b^\psi \right) \cdot \tilde{\nabla} \tilde{\Delta}_\lambda^2 - \left(\Delta_a \delta \mathbf{U}_a^\psi - \Delta_b \delta \mathbf{U}_b^\psi \right) \cdot \tilde{\nabla} \tilde{\Delta}_\lambda \right] S_E^{\theta\theta} \\ & - \beta \left[\partial_{\tilde{x}} \left(\tilde{\Delta}_\lambda + \frac{1}{4}\bar{\Delta} \right) - 2\partial_{\tilde{x}} \Gamma \right] \delta S^{\theta\theta} - 2 \left[\left(\tilde{\Delta}_\lambda + \frac{1}{4}\bar{\Delta} \right) \left(\tilde{\Delta} + \frac{1}{4}\bar{\Delta} \right) - \Gamma^2 \right] \delta S^{\theta\theta}, \end{aligned} \quad (\text{A } 6)$$

where $\Gamma \stackrel{\text{def}}{=} \partial_{\tilde{x}}^2 \bar{x} + \partial_{\tilde{y}}^2 \bar{y}$, and operators with tildes indicate differentiation with respect to $\tilde{\mathbf{x}} = \mathbf{x}_a - \mathbf{x}_b$ while operators with overbars indicate differentiation with respect to $\bar{\mathbf{x}} = (\mathbf{x}_a + \mathbf{x}_b)/2$.

Because of the statistical homogeneity of the equilibrium state, the eigenfunctions are sinusoidal and the coherent flow component of the eigenfunctions are $[\delta\Psi, \delta\Theta] = [a_\psi, a_\theta] e^{i\mathbf{n} \cdot \mathbf{x}} e^{\sigma t}$, with covariance components:

$$[\delta S^{\psi\psi}, \delta S^{\psi\theta}, \delta S^{\theta\psi}, \delta S^{\theta\theta}]^T = \frac{e^{i\mathbf{n} \cdot \bar{\mathbf{x}}} e^{\sigma t}}{2\pi} \int_{-\infty}^{\infty} \int_{-\infty}^{\infty} [\hat{S}^{\psi\psi}, \hat{S}^{\psi\theta}, \hat{S}^{\theta\psi}, \hat{S}^{\theta\theta}]^T e^{i\mathbf{k} \cdot \bar{\mathbf{x}}} d^2 \mathbf{k}. \quad (\text{A } 7)$$

Inserting the eigenfunction into (A 3)-(A 6), we determine the perturbation covariance amplitudes in terms of the amplitudes of the perturbation mean flow. They are given by:

$$\hat{S}^{\psi\psi} = \frac{a_\psi \hat{\mathbf{z}} \cdot (\mathbf{k}_+ \times \mathbf{n}) k_+^2 (k_+^2 - N^2) \hat{S}_{E+}^{\psi\psi}}{(\sigma + 2) k_+^2 k_-^2 + i\beta (k_x - k_+^2 - k_{x+} k_-^2)} - \frac{a_\psi \hat{\mathbf{z}} \cdot (\mathbf{k}_- \times \mathbf{n}) k_-^2 (k_-^2 - N^2) \hat{S}_{E-}^{\psi\psi}}{(\sigma + 2) k_+^2 k_-^2 + i\beta (k_x - k_+^2 - k_{x+} k_-^2)}, \quad (\text{A } 8a)$$

$$\hat{S}^{\psi\theta} = \frac{a_\theta \hat{\mathbf{z}} \cdot (\mathbf{k}_+ \times \mathbf{n}) k_+^2 (k_+^2 - n_\lambda^2) \hat{S}_{E+}^{\psi\psi}}{(\sigma + 2) k_+^2 k_{\lambda-}^2 + i\beta (k_x - k_+^2 - k_{x+} k_{\lambda-}^2)} - \frac{a_\theta \hat{\mathbf{z}} \cdot (\mathbf{k}_- \times \mathbf{n}) k_-^2 (k_-^2 - n^2) \hat{S}_{E-}^{\theta\theta}}{(\sigma + 2) k_+^2 k_{\lambda-}^2 + i\beta (k_x - k_+^2 - k_{x+} k_{\lambda-}^2)}, \quad (\text{A } 8b)$$

$$\hat{S}^{\theta\psi} = \frac{a_\theta \hat{\mathbf{z}} \cdot (\mathbf{k}_+ \times \mathbf{n}) k_{\lambda+}^2 (k_+^2 - n^2) \hat{S}_{E+}^{\theta\theta}}{(\sigma + 2) k_{\lambda+}^2 k_-^2 + i\beta (k_x - k_{\lambda+}^2 - k_{x+} k_-^2)} - \frac{a_\theta \hat{\mathbf{z}} \cdot (\mathbf{k}_- \times \mathbf{n}) k_-^2 (k_-^2 - n_\lambda^2) \hat{S}_{E-}^{\psi\psi}}{(\sigma + 2) k_{\lambda+}^2 k_-^2 + i\beta (k_x - k_{\lambda+}^2 - k_{x+} k_-^2)}, \quad (\text{A } 8c)$$

$$\hat{S}^{\theta\theta} = \frac{a_\psi \hat{\mathbf{z}} \cdot (\mathbf{k}_+ \times \mathbf{n}) k_{\lambda+}^2 (k_{\lambda+}^2 - n^2) \hat{S}_{E+}^{\theta\theta}}{(\sigma + 2) k_{\lambda+}^2 k_{\lambda-}^2 + i\beta (k_x - k_{\lambda+}^2 - k_{x+} k_{\lambda-}^2)} - \frac{a_\psi \hat{\mathbf{z}} \cdot (\mathbf{k}_- \times \mathbf{n}) k_{\lambda-}^2 (k_{\lambda-}^2 - n^2) \hat{S}_{E-}^{\theta\theta}}{(\sigma + 2) k_{\lambda+}^2 k_{\lambda-}^2 + i\beta (k_x - k_{\lambda+}^2 - k_{x+} k_{\lambda-}^2)}, \quad (\text{A } 8d)$$

with the notation $\mathbf{k}_\pm = \mathbf{k} \pm \mathbf{n}/2$, $k_\pm^2 = |\mathbf{k}_\pm|^2$, $k_{\lambda\pm}^2 = |\mathbf{k}_\pm|^2 + 2\lambda^2$, $n_\lambda = n^2 + 2\lambda^2$, $\hat{S}_{E\pm}^{\psi\psi}(\mathbf{k}) = (1+p)\hat{\hat{\mathbf{e}}}(\mathbf{k}_\pm)/2k_\pm^4$, $\hat{S}_{E\pm}^{\theta\theta}(\mathbf{k}) = (1-p)\hat{\hat{\mathbf{e}}}(\mathbf{k}_\pm)/2k_{\lambda\pm}^4$ and $\hat{\mathbf{z}}$ the unit vector representing the vertical direction.

The perturbation eddy stress divergences can then be determined as a function of the perturbation coherent flow and the spectrum of the excitation. They are:

$$[\delta f_\psi, \delta f_\theta]^T = [a_\psi (f_{\psi\psi+} - f_{\psi\psi-}), a_\theta (f_{\theta\theta+} - f_{\theta\theta-})]^T e^{i\mathbf{n} \cdot \mathbf{x}}, \quad (\text{A } 9)$$

where

$$\begin{aligned} f_{\psi\psi\pm} &= \frac{1}{4\pi} \int_{-\infty}^{\infty} \int_{-\infty}^{\infty} \frac{\hat{\mathbf{z}} \cdot [k_+^2 (\mathbf{k}_- \times \mathbf{n}) - k_-^2 (\mathbf{k}_+ \times \mathbf{n})] \hat{\mathbf{z}} \cdot (\mathbf{k}_\pm \times \mathbf{n}) k_{\lambda\pm}^2 (k_{\lambda\pm}^2 - n^2) \hat{S}_{E\pm}^{\theta\theta}}{(\sigma + 2) k_{\lambda+}^2 k_{\lambda-}^2 + i\beta (k_x - k_{\lambda+}^2 - k_{x+} k_{\lambda-}^2)} d^2 \mathbf{k} \\ &+ \frac{1}{4\pi} \int_{-\infty}^{\infty} \int_{-\infty}^{\infty} \frac{\hat{\mathbf{z}} \cdot [k_+^2 (\mathbf{k}_- \times \mathbf{n}) - k_-^2 (\mathbf{k}_+ \times \mathbf{n})] \hat{\mathbf{z}} \cdot (\mathbf{k}_\pm \times \mathbf{n}) k_\pm^2 (k_\pm^2 - N^2) \hat{S}_{E\pm}^{\psi\psi}}{(\sigma + 2) k_+^2 k_-^2 + i\beta (k_x - k_+^2 - k_{x+} k_-^2)} d^2 \mathbf{k} \quad (\mathbf{A}^2 \mathbf{k}) \\ f_{\theta\theta\pm} &= \frac{1}{4\pi} \int_{-\infty}^{\infty} \int_{-\infty}^{\infty} \frac{\hat{\mathbf{z}} \cdot [-k_{\lambda\mp}^2 (\mathbf{k}_\pm \times \mathbf{n}) + k_\pm^2 (\mathbf{k}_\mp \times \mathbf{n})] \hat{\mathbf{z}} \cdot (\mathbf{k}_\pm \times \mathbf{n}) k_\pm^2 (k_\pm^2 - n_\lambda^2) \hat{S}_{E\pm}^{\psi\psi}}{(\sigma + 2) k_+^2 k_{\lambda-}^2 + i\beta (k_x - k_+^2 - k_{x+} k_{\lambda-}^2)} d^2 \mathbf{k} \\ &+ \frac{1}{4\pi} \int_{-\infty}^{\infty} \int_{-\infty}^{\infty} \frac{\hat{\mathbf{z}} \cdot [-k_\mp^2 (\mathbf{k}_\pm \times \mathbf{n}) + k_{\lambda\pm}^2 (\mathbf{k}_\mp \times \mathbf{n})] \hat{\mathbf{z}} \cdot (\mathbf{k}_\pm \times \mathbf{n}) k_{\lambda\pm}^2 (k_{\lambda\pm}^2 - n^2) \hat{S}_{E\pm}^{\theta\theta}}{(\sigma + 2) k_{\lambda+}^2 k_-^2 + i\beta (k_x - k_{\lambda+}^2 - k_{x+} k_-^2)} d^2 \mathbf{k} \quad (\mathbf{A}^2 \mathbf{k}) \end{aligned}$$

Note that when there is no correlation of the barotropic and the baroclinic streamfunction at equilibrium ($S_E^{\psi\theta} = S_E^{\theta\psi} = 0$), perturbations to the homogeneous equilibrium with no temperature difference across the channel have the property that barotropic mean flow perturbations induce only barotropic mean flow accelerations and baroclinic mean flow perturbations induce only baroclinic mean flow accelerations decoupling the barotropic and baroclinic mean flow tendencies.

A further reduction in the above expressions can be achieved, as noted by Srinivasan & Young (2012), by utilizing the exchange symmetry of the covariance $\mathbf{C}(\mathbf{x}_a, \mathbf{x}_b) = \mathbf{C}(\mathbf{x}_b, \mathbf{x}_a)^T$, by changing the sign of \mathbf{k} in the integrals to obtain

$$f_{\psi\psi+} = -f_{\psi\psi-}, \quad f_{\theta\theta+} = -f_{\theta\theta-}. \quad (\text{A } 12)$$

Introduction of (A 12) into (A 9) and the change of variables $\mathbf{k} \rightarrow \mathbf{k} + \mathbf{n}/2$, in the integrals

yields the more compact representation of the eddy stress divergences:

$$[\delta f_\psi, \delta f_\theta]^T = [a_\psi f_\psi(\sigma), a_\theta f_\theta(\sigma)]^T e^{i\mathbf{n} \cdot \mathbf{x}} , \quad (\text{A } 13)$$

with

$$\begin{aligned} f_\psi(\sigma) = & \frac{1}{2\pi n^2} \int_{-\infty}^{\infty} \int_{-\infty}^{\infty} \frac{(n_y k_x - n_x k_y)^2 (k_{++}^2 - k^2) k^2 (k^2 - n^2) \hat{S}_E^{\psi\psi}}{(\sigma + 2) k^2 k_{++}^2 + i\beta(k_x k_{++}^2 - k_{x++} k^2)} d^2 \mathbf{k} \\ & + \frac{1}{2\pi n^2} \int_{-\infty}^{\infty} \int_{-\infty}^{\infty} \frac{(n_y k_x - n_x k_y)^2 (k_{++}^2 - k^2) k_\lambda^2 (k_\lambda^2 - n^2) \hat{S}_E^{\theta\theta}}{(\sigma + 2) k_\lambda^2 k_{\lambda++}^2 + i\beta(k_x k_{\lambda++}^2 - k_{x++} k_\lambda^2)} d^2 \mathbf{k} , \end{aligned} \quad (\text{A } 14)$$

and

$$\begin{aligned} f_\theta(\sigma) = & \frac{1}{2\pi n_\lambda^2} \int_{-\infty}^{\infty} \int_{-\infty}^{\infty} \frac{(n_y k_x - n_x k_y)^2 (k_{\lambda++}^2 - k^2) k^2 (k^2 - n_\lambda^2) \hat{S}_E^{\psi\psi}}{(\sigma + 2) k^2 k_{\lambda++}^2 + i\beta(k_x k_{\lambda++}^2 - k_{x++} k^2)} d^2 \mathbf{k} \\ & + \frac{1}{2\pi n_\lambda^2} \int_{-\infty}^{\infty} \int_{-\infty}^{\infty} \frac{(n_y k_x - n_x k_y)^2 (k_{++}^2 - k_\lambda^2) k_\lambda^2 (k_\lambda^2 - n^2) \hat{S}_E^{\theta\theta}}{(\sigma + 2) k_\lambda^2 k_{++}^2 + i\beta(k_x k_{++}^2 - k_{x++} k_\lambda^2)} d^2 \mathbf{k} , \end{aligned} \quad (\text{A } 15)$$

with the notation: $\mathbf{k}_{++} = \mathbf{k} + \mathbf{n}$, $k_{++}^2 = |\mathbf{k}_{++}|^2$ and $k_{\lambda++}^2 = |\mathbf{k}_{++}|^2 + 2\lambda^2$.

Because the barotropic and baroclinic perturbation components decouple upon substitution of (A 13) in (A 2) we obtain that either σ satisfies:

$$\sigma + 1 - i\beta n_x / n^2 = f_\psi(\sigma) , \quad (\text{A } 16)$$

and the eigenfunction is purely barotropic with $a_\psi \neq 0$ and $a_\theta = 0$, or that σ satisfies:

$$\sigma + 1 - i\beta n_x / n_\lambda^2 = f_\theta(\sigma) , \quad (\text{A } 17)$$

and the eigenfunction is purely baroclinic with $a_\psi = 0$ and $a_\theta \neq 0$.

REFERENCES

- AIT-CHAALAL, F., SCHNEIDER, T., MEYER, B. & MARSTON, J. B. 2016 Cumulant expansions for atmospheric flows. *New. J. Phys.* **18** (2), 025019.
- BAKAS, N. A., CONSTANTINOU, N. C. & IOANNOU, P. J. 2015 S3T stability of the homogeneous state of barotropic beta-plane turbulence. *J. Atmos. Sci.* **72** (5), 1689–1712.
- BAKAS, N. A. & IOANNOU, P. J. 2013*a* Emergence of large scale structure in barotropic β -plane turbulence. *Phys. Rev. Lett.* **110**, 224501.
- BAKAS, N. A. & IOANNOU, P. J. 2013*b* On the mechanism underlying the spontaneous emergence of barotropic zonal jets. *J. Atmos. Sci.* **70** (7), 2251–2271.
- BAKAS, N. A. & IOANNOU, P. J. 2014 A theory for the emergence of coherent structures in beta-plane turbulence. *J. Fluid Mech.* **740**, 312–341.
- BAKAS, N. A. & IOANNOU, P. J. 2019 Emergence of non-zonal coherent structures. In *Zonal jets* (ed. B. Galperin & P. L. Read), chap. 27. Cambridge University Press, (arXiv:1501.05280).
- BERNSTEIN, J. & FARRELL, B. F. 2010 Low frequency variability in a turbulent baroclinic jet: Eddy–mean flow interactions in a two-level model. *J. Atmos. Sci.* **67** (2), 452–467.
- BOUCHET, F., MARSTON, J. B. & TANGARIFE, T. 2018 Fluctuations and large deviations of Reynolds stresses in zonal jet dynamics. *Phys. Fluids* **30** (1), 015110.
- BUSSE, F. H. 1976 A simple model of convection in the jovian atmosphere. *Icarus* **29**, 255–260.
- CEHELSKY, P. & TUNG, K.-K. 1991 Nonlinear baroclinic adjustment. *J. Atmos. Sci.* **48**, 1930–1947.
- CHO, J. Y.-K. & POLVANI, L. M. 1996 The emergence of jets and vortices in freely evolving, shallow-water turbulence on a sphere. *Phys. Fluids* **8** (6), 1531–1552.
- CONSTANTINOU, N. C., FARRELL, B. F. & IOANNOU, P. J. 2014*a* Emergence and equilibration of jets in beta-plane turbulence: applications of Stochastic Structural Stability Theory. *J. Atmos. Sci.* **71** (5), 1818–1842.

- CONSTANTINO, N. C., FARRELL, B. F. & IOANNOU, P. J. 2016 Statistical state dynamics of jet-wave coexistence in barotropic beta-plane turbulence. *J. Atmos. Sci.* **73** (5), 2229–2253.
- CONSTANTINO, N. C., LOZANO-DURÁN, A., NIKOLAIDIS, M.-A., FARRELL, B. F., IOANNOU, P. J. & JIMÉNEZ, J. 2014*b* Turbulence in the highly restricted dynamics of a closure at second order: comparison with DNS. *J. Phys. Conf. Ser.* **506**, 012004.
- DELSOLE, T. 1996 Can quasigeostrophic turbulence be modeled stochastically? *J. Atmos. Sci.* **53**, 1617–1633.
- FARRELL, B. F., GAYME, D. F. & IOANNOU, P. J. 2017 A statistical state dynamics approach to wall-turbulence. *Phil. Trans. R. Soc. A* **375** (2089), 20160081.
- FARRELL, B. F. & IOANNOU, P. J. 2003 Structural stability of turbulent jets. *J. Atmos. Sci.* **60**, 2101–2118.
- FARRELL, B. F. & IOANNOU, P. J. 2007 Structure and spacing of jets in barotropic turbulence. *J. Atmos. Sci.* **64**, 3652–3665.
- FARRELL, B. F. & IOANNOU, P. J. 2008 Formation of jets by baroclinic turbulence. *J. Atmos. Sci.* **65**, 3353–3375.
- FARRELL, B. F. & IOANNOU, P. J. 2009*a* Emergence of jets from turbulence in the shallow-water equations on an equatorial beta plane. *J. Atmos. Sci.* **66**, 3197–3207.
- FARRELL, B. F. & IOANNOU, P. J. 2009*b* A stochastic structural stability theory model of the drift wave-zonal flow system. *Phys. Plasmas* **16**, 112903.
- FARRELL, B. F. & IOANNOU, P. J. 2017 Statistical state dynamics based theory for the formation and equilibration of Saturn’s north polar jet. *Phys. Rev. Fluids* **2** (7), 073801.
- FARRELL, B. F. & IOANNOU, P. J. 2019 Statistical State Dynamics: a new perspective on turbulence in shear flow. In *Zonal jets* (ed. B. Galperin & P. L. Read), chap. 25. Cambridge University Press, (arXiv:1412.8290).
- FARRELL, B. F., IOANNOU, P. J., JIMÉNEZ, J., CONSTANTINO, N. C., LOZANO-DURÁN, A. & NIKOLAIDIS, M.-A. 2016 A statistical state dynamics-based study of the structure and mechanism of large-scale motions in plane Poiseuille flow. *J. Fluid Mech.* **809**, 290–315.
- FITZGERALD, J. G. & FARRELL, B. F. 2014 Mechanisms of mean flow formation and suppression in two-dimensional Rayleigh-Bénard convection. *Phys. Fluids* **26** (5), 054104.
- FRISCH, U. 1995 *Turbulence: The Legacy of A. N. Kolmogorov*. Cambridge University Press.
- FRISHMAN, A. & HERBERT, C. 2018 Turbulence statistics in a 2D vortex condensate. *Phys. Rev. Lett.* **120**, 204505.
- GALPERIN, B., SUKORIAN, S., DIKOVSKAYA, N., READ, P. L., YAMAZAKI, Y. H. & WORDSWORTH, R. 2006 Anisotropic turbulence and zonal jets in rotating flows with a beta - effect. *Nonlin. Processes Geophys.* **13**, 83–98.
- GALPERIN, B., YOUNG, R. M. B., SUKORIAN, S., DIKOVSKAYA, N., READ, P. L., LANCASTER, A. L. & ARMSTRONG, D. 2014 Cassini observations reveal a regime of zonostrophic macroturbulence on Jupiter. *Icarus* **229**, 295–320.
- HELD, I. M. & LARICHEV, V. D. 1996 A scaling theory for horizontally homogeneous, baroclinically unstable flow on a beta plane. *J. Atmos. Sci.* **53**, 946–952.
- HERRING, J. R. 1963 Investigation of problems in thermal convection. *J. Atmos. Sci.* **20**, 325–338.
- HOPF, E. 1952 Statistical hydromechanics and functional calculus. *J. Ration. Mech. Anal.* **1**, 87–123.
- INGERSOLL, A. P. 1990 Atmospheric dynamics of the outer planets. *Science* **248**, 308–315.
- KASPI, Y. H. & FLIERL, G. R. 2007 Formation of jets by baroclinic instability on gas planet atmospheres. *J. Atmos. Sci.* **64**, 3177–3194.
- KASPI, Y. H., FLIERL, G. R. & SHOWMAN, A. P. 2009 The deep wind structure of the giant planets: Results from an anelastic general circulation model. *Icarus* **202**, 525–542.
- KRAICHNAN, R. H. 1964 Direct Interaction Approximation for shear and thermally driven turbulence. *Phys. Fluids* **7**, 1048–1062.
- LILLY, D. K. 1969 Numerical simulation of two-dimensional turbulence. *Phys. Fluids* **12**, II240–II249.
- LIU, J. & SCHNEIDER, T. 2010 Mechanisms of jet formation on the giant planets. *Jas* **67** (1), 3652–3672.
- MARSTON, J. B. 2010 Statistics of the general circulation from cumulant expansions. *Chaos* **20**, 041107.

- MARSTON, J. B., CHINI, G. P. & TOBIAS, S. M. 2016 Generalized quasilinear approximation: Application to zonal jets. *Phys. Rev. Lett.* **116** (21), 214501 EP –5.
- MARSTON, J. B., CONOVER, E. & SCHNEIDER, T. 2008 Statistics of an unstable barotropic jet from a cumulant expansion. *J. Atmos. Sci.* **65** (6), 1955–1966.
- MAXIMENKO, N. A., BANG, B. & SASAKI, H. 2005 Observational evidence of alternating zonal jets in the world ocean. *Geophys. Res. Lett.* **32**, L12607.
- MONIN, A. S. & YAGLOM, A. M. 1973 *Statistical Fluid Mechanics: Mechanics of Turbulence*, vol. 1. The MIT Press.
- PARKER, J. B. & KROMMES, J. A. 2013 Zonal flow as pattern formation. *Phys. Plasmas* **20**, 100703.
- PARKER, J. B. & KROMMES, J. A. 2014 Generation of zonal flows through symmetry breaking of statistical homogeneity. *New J. Phys.* **16** (3), 035006.
- PARKER, J. B. & KROMMES, J. A. 2015 Zonal flow as pattern formation. In *Zonal jets: Phenomenology, genesis, physics* (ed. B. Galperin & P. L. Read), chap. 5. Cambridge University Press.
- RHINES, P. B. 1975 Waves and turbulence on a beta-plane. *J. Fluid Mech.* **69**, 417–433.
- SÁNCHEZ-LAVEGA, A., SROMOVSKY, L. A., SHOWMAN, A. P., DELGENIO, A.D., YOUNG, R. M. B., HUESO, R., GARCIA-MELENDO, E., KASPI, Y., ORTON, G. S., BARRADO-IZAGIRRE, N., CHOI, D. S. & BARBARA, J. M. 2019 Gas giants. In *Zonal jets* (ed. B. Galperin & P. L. Read), chap. 4. Cambridge University Press, (arXiv:1501.05280).
- SCOTT, R. K. & DRITSCHEL, D. G. 2012 The structure of zonal jets in geostrophic turbulence. *J. Fluid Mech.* **711**, 576–598.
- SCOTT, R. K. & POLVANI, L. M. 2007 Forced-dissipative shallow-water turbulence on the sphere and the atmospheric circulation of the giant planets. *J. Atmos. Sci.* **64**, 3158–3176.
- SHOWMAN, ADAM P 2007 Numerical Simulations of Forced Shallow-Water Turbulence: Effects of Moist Convection on the Large-Scale Circulation of Jupiter and Saturn. *J. Atmos. Sci.* **64** (9), 3132–3157.
- SRINIVASAN, K. & YOUNG, W. R. 2012 Zonostrophic instability. *J. Atmos. Sci.* **69** (5), 1633–1656.
- THOMSON, S. I. & MCINTYRE, MICHAEL E. 2014 Jupiter’s unearthly jets: a new turbulent model exhibiting statistical steadiness without large-scale dissipation. *jas* **73**, 1119–1141.
- TOBIAS, S. M., DAGON, K. & MARSTON, J. B. 2011 Astrophysical fluid dynamics via direct numerical simulation. *Astrophys. J.* **727**, 127.
- VALLIS, G. K. & MALTRUD, M. E. 1993 Generation of mean flows and jets on a beta-plane and over topography. *J. Phys. Oceanogr.* **23**, 1346–1362.
- VASAVADA, A. R. & SHOWMAN, A. P. 2005 Jovian atmospheric dynamics: an update after *Galileo* and *Cassini*. *Rep. Prog. Phys.* **68**, 1935–1996.
- WILLIAMS, G. P. 1978 Planetary circulations: 1. Barotropic representation of Jovian and terrestrial turbulence. *J. Atmos. Sci.* **35** (8), 1399–1426.
- WILLIAMS, G. P. 2003 Jet sets. *J. Meteorol. Soc. Jpn. Ser. II* **81** (3), 439–476.